Thin Optic Surface Analysis for High Resolution X-ray Telescopes

by

Mireille Akilian

B.E., Mechanical Engineering, American University of Beirut (2002)

Submitted to the Department of Mechanical Engineering
in partial fulfillment of the requirements for the degree of

Master of Science in Mechanical Engineering

at the

MASSACHUSETTS INSTITUTE OF TECHNOLOGY

September 2004

Author .....
Department of Mechanical Engineering
August 6, 2004

Certified by .....
Mark L. Schattenburg
Senior Research Scientist
Thesis Supervisor

Certified by .....
Samir Nayfeh
Assistant Professor, Mechanical Engineering
Thesis Supervisor

Accepted by .....
Ain A. Sonin
Chairman, Department Committee on Graduate Students

Thin Optic Surface Analysis for High Resolution X-ray Telescopes

by

Mireille Akilian

Submitted to the Department of Mechanical Engineering
on August 6, 2004, in partial fulfillment of the
requirements for the degree of
Master of Science in Mechanical Engineering

Abstract

The art of glass developed throughout the years has covered artifacts ranging from crude ornaments to high precision optics used in flat panel displays, hard disk drives, and x-ray telescopes. Methods for manufacturing glass sheets and further sheet shaping processes are covered. Future generation, high resolution x-ray telescopes require thin optics with large surface area to thickness ratio and a surface flatness of ~500 nm. A novel method utilizing porous ceramics, which provide a thin layer of air for sheet glass to rest on during the shaping process, is investigated. The shaping process involves slumping glass on a uniform layer of air at elevated temperatures, where the viscosity of glass is low enough for it to sag under its own weight and replicate the surface it rests on.

Flow in porous, rectangular air bearings is covered with both flat and grooved surfaces. The pressure distribution in the air gap between the ceramic and the glass sheet determines the surface quality of glass during slumping. The mechanical integrity of porous ceramics at elevated temperatures is investigated to predict the effect of the decrease in ceramic stiffness on the final shape of the optic.

A metrology truss used to kinematically constrain thin optics during metrology is designed. This device mitigates the effects of external forces, such as gravity, friction, and thermal stresses, induced on the optic while being mechanically constrained, thus significantly improving the repeatability of the optic surface map measurements.

Thesis Supervisor: Mark L. Schattenburg
Title: Senior Research Scientist

Thesis Supervisor: Samir Nayfeh
Title: Assistant Professor, Mechanical Engineering

Acknowledgments

My beautiful sisters, Nathalie and Kathia, and my parents, Edith and Krikor, you have been my inspiration. I wish to thank Paul, Rozina, and Richard Daoud for looking after me even though they were thousands of miles away. I will never forget their kindness.

I am thankful to Marie-Anne, Naji, Ramy, Charles, John, and Wassim for guiding me throughout the past two years.

Chi, you are simply the best. You have helped me put things in perspective on so many levels, but most of all, thank you for listening to me during the hardest period when I was struggling with absolute ignorance. I would like to thank Juan Montoya, Chulmin Joo, Yanxia Sun, Alexandre Lamure, and Andy Lapsa for their encouragement and contributions, Craig and Laura Forest for helping me stay focused on many occasions, Ray Schuzzarella and Teresa Santiago for locating the equipment I needed, Ralf Heilmann, Bob Fleming and Ed Murphy for their help, and both the MIT and CSR Machine Shop staff for all their services, particularly Peter Morley for putting up with my deadlines.

I would also like to thank Hyun and Waty for brining out the beauty of this place, and Jephte, my Tae Kwon Do coach, for reminding me that there is life outside MIT boundaries.

I genuinely appreciate the efforts of Shoumen Datta, Buck Heidrick, Samir Nayfeh, Alexander Slocum, and David Trumper. Their insights paved my way.

Mark Schattenburg, I hope I grow to be as diligent, creative and diverse as you are. To you, I am eternally grateful.

Contents

List of Figures

List of Tables

Chapter 1

Glass

"An inorganic product of fusion which has cooled to a rigid state without crystallizing" [1], one of the many definitions of glass that have been around for over sixty years. Glass, no longer restricted to inorganic substances, is a material with amorphous or liquid-like structures that behaves as a solid at low temperatures. The reversible transition from liquid to non-crystalline solid upon cooling occurs over a narrow interval of temperatures identified as the glass temperature T_g. Properties of glass such as density, viscosity, thermal conductivity, and heat capacity can be altered reversibly within this interval by suitable heat treatment; thus, these properties depend on thermal history and not just current temperature.

Amorphous glass is isotropic with no internal grain boundaries or structural elements lying in specific directions. It is the liquid-like structure of glass that gives it its special properties. The most important characteristic of glass is the rapid change of its viscosity with a change in temperature. This property is the key parameter in glass formation: as the temperature of glass is raised, its viscosity decreases; however, glass is more viscous than other common materials at this elevated temperature, but it still can flow with ease under gravity or other relatively low stresses. Glass shows a Newtonian behavior, which means that in isothermal states, the rate of flow is proportional to the shear stress. This allows for glass to be drawn down to thin sheets or small diameter tubes without necking and consequent fracture. As the temperature is decreased, glass acts as an elastic solid.

Atomic structures in glass are mostly covalently bonded, which means that glass has a theoretical high strength; however, the presence of surface scratches and dents makes glass weak and brittle in practice. Retaining the theoretical strength of glass depends on the quality of the surface and how well surface damage can be controlled. The lack of grain boundaries in amorphous glass allows for a crack initiated at one end to propagate through the entire thickness of the glass. Therefore, in the cases where mechanical strength is important, fine-grained glass ceramics are preferred.

1.1 Sheet Glass

Thin glass substrates are used in various fields including optoelectronics, hard-disk drive industry, photomasks in the semiconductor industry, and hard pellicles for 157 nm lithography [2]. Perhaps the most important industrial application for sheet glass is the high-performance flat panel displays used in portable computers, pocket televisions, cellular phones, and high-resolution monochrome workstation displays.

Flat panel display technology provides a higher display size for a given weight and physical dimensions than cathode ray tube technology, allowing for high information content screens with large areas to be used in size-limited places. Commercially available sheet glass places a major constraint on the absolute potential of flat panel display technology. Liquid crystal displays require two sheets of glass separated by a critical gap of 5-10 μm. This gap is known as the cell spacing. Glass warp causes variations in cell spacing, which leads to the deviation of the electric field in that region from the surrounding pixels resulting in a non-uniform color [1]. This tight dimensional tolerance becomes a challenge when commercially available glass has a surface flatness up to 600 μm. Surface flatness is usually mistaken for total thickness variation. Figure 1-1 helps understand the difference between the two characteristics. The application of interest in this thesis is optics for high resolution X-ray telescopes, where foil optics are to replace monolithic mirrors used previously in the *Chandra* X-ray Telescope.

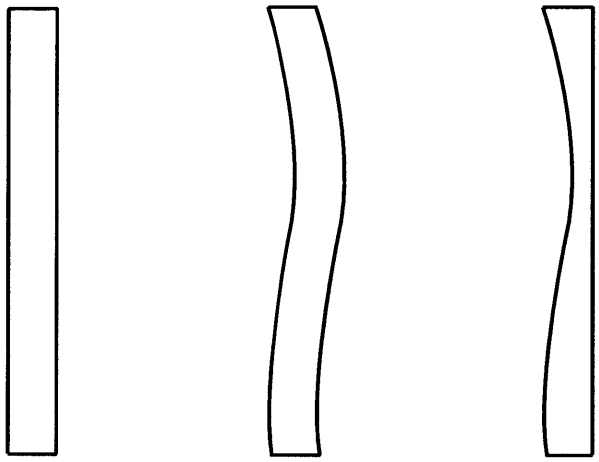

Figure 1-1: The difference between total thickness variation and surface flatness. *(a)* shows a perfect, thin optic, *(b)* shows an optic with a uniform thickness but poor surface flatness, and *(c)* shows an optic with a flat right surface but a large total thickness variation.

1.2 Sheet Glass for X-ray Telescopes

X-ray astronomy has been the gateway for knowledge about the universe. X-rays are produced when the temperature of matter reaches millions of degrees as a result of explosions, high magnetic fields, or extreme gravitational forces. The information gathered from X-rays can help scientists answer questions related to the origin and future of the universe.

Due to their high energy and consequently short wavelengths, X-rays are easily absorbed by matter. The atmosphere being the primary barrier absorbing X-rays reaching the earth, X-ray telescopes must be launched into space, placing additional difficulties on the electronics and optics of the telescope that must withstand take-off vibrations and the harsh environment.

Of the various X-ray telescopes launched into space, NASA's *Chandra* X-ray Observatory is the most significant when it comes to resolution and range of vision. *Chandra* utilizes sets of nested monolithic mirrors in the Wolter I configuration, as

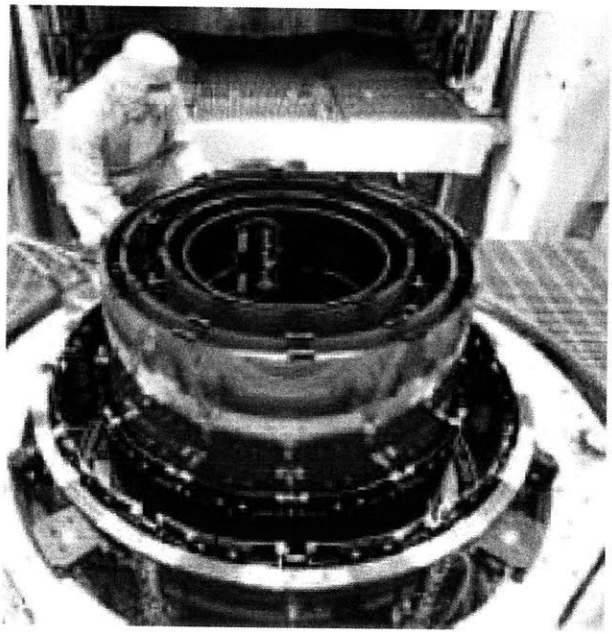

Figure 1-2: Monolithic optics used in NASA's *Chandra* X-ray telescope.

shown in Figure 1-2. X-rays hit the mirror surfaces at shallow incident angles to reflect off and converge at the telescope focal point, as shown in Figure 1-3. Extreme demands are placed on the optics used in order to obtain a high resolution image. The mirrors are divided into paraboloids and hyperboloids with an overall focal length of 10 m and are fabricated using standard grinding and polishing processes to obtain a surface smoothness of a few atoms and provide an overall resolution of $\sim$0.5 arcsec. Figure 1-4 shows pictures obtained from *Chandra*. Due to the heavy weight of the monolithic optics, only four sets of mirrors were launched, providing an overall effective collecting area of 800 cm^2. A larger collecting area on the order of 10-100 times that of *Chandra* is necessary if distant and faint objects are to be observed.

Sheet optics have been used in X-ray telescopes such as the *X-ray Multi-Mirror (XMM)* launched by the European Space Agency, and *ASTRO-E*, which was a joint launch between Japan and the US. Both telescopes use thousands of foil optics assembled in modules to form a large number of nested shells, as shown in Figure 1-5. This leads to an increase in the effective collecting area at a much lower weight when compared to the monolithic mirrors. The cost of manufacturing thin optics is greatly

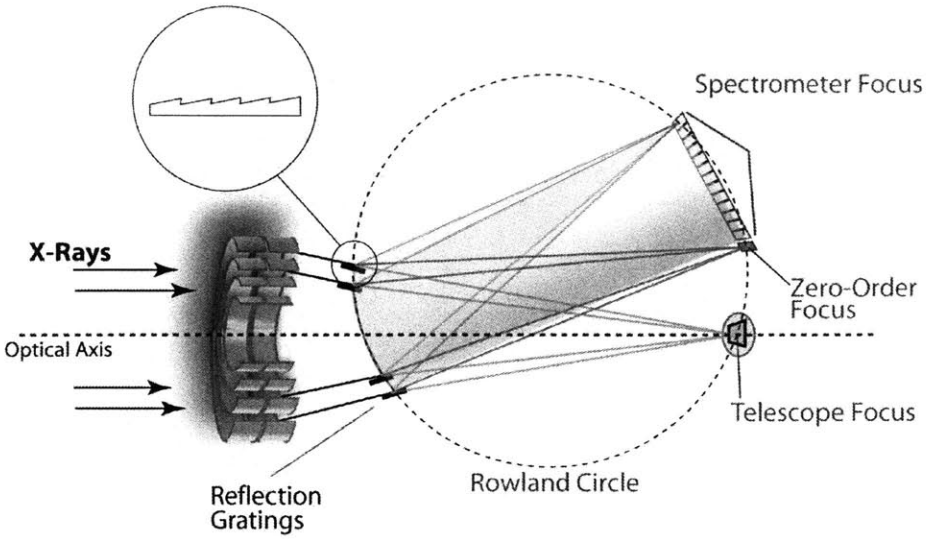

Figure 1-3: X-rays reflecting off Wolter I type optics and converging at the telescope focus. Reflection gratings intercept part of the X-rays and focus them on the Rowland circle to perform spectroscopy on the incoming beam.

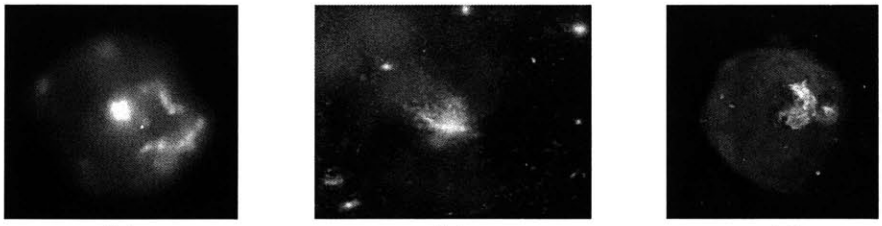

Figure 1-4: Pictures from the *Chandra* X-ray telescope. *(a)* shows a massive star explosion 160,000 light years away, *(b)* shows a galaxy being torn apart as it travels at approximately 4.5 million miles an hour, and *(c)* shows the supernova remnant *N63A* in a nearby galaxy [3].

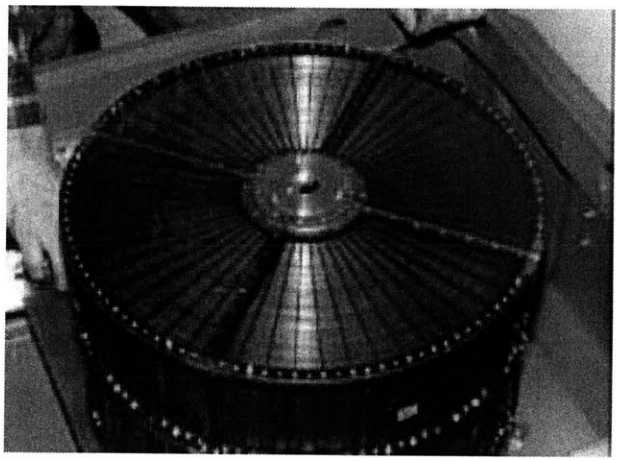

Figure 1-5: Thousands of thin optics assembled in the Wolter I configuration.

reduced; however, such optics have not been able to provide the same resolution as the monolithic ones in *Chandra*. The resolution ranges between 15 and 110 arcsec for XMM and AstroE, respectively.

NASA's future missions including the *Constellation X* and *High Resolution X-ray Spectroscopy Mission* will use thin optics for both reflecting mirrors and spectrometers. The required resolution must match that of *Chandra's*. Optics of interest are $100 \times 140 - 200 \times 0.4$ mm^3 in size with a surface flatness of ~ 0.5 μm to provide a resolution of 1 arcsec.

1.3 Sheet Glass Manufacturing Processes

The basic process for manufacturing sheet glass is the float process, where molten glass at elevated temperatures (around 1000°C) is poured continuously out of a furnace and onto a level bath of molten tin. The glass floats on the tin and spreads out to replicate the tin surface. Thicknesses ranging from 0.55 to 25 mm [4] can be achieved by controlling the speed at which the solidifying glass is drawn off from the tin bath. Major drawbacks include tin residues found on the surface in contact with the tin bath, and bow and warp introduced due to lower ion exchange levels on the tin side than the air side of float glass [5].

The slot-draw process can be used to form thin sheets by drawing hot glass through a slot with accurate dimensions, as shown in Figure 1-6. The outside surface comes in contact with two pulling rollers reducing surface quality. Dimensional control is compromised throughout the process, and the final glass has surface warp exceeding the requirements. A redrawing procedure can be utilized to manufacture thin glass with tighter dimensional tolerances, as shown in Figure 1-7, by first drawing a mother glass plate, inserting it into a redraw furnace to heat it to a temperature corresponding to a viscosity of 10^7 to 10^{11} poise, and then thinning the plate to the desired thickness. In an attempt to reduce contact of the outside surface of the glass sheet with the forming apparatus, Corning developed a fusion process, where glass is delivered to a trough at the top of a pipe to overflow the pipe on both sides and reunite at the bottom, as shown in Figure 1-8. This process can be used to manufacture glass to less than 0.5 mm, depending on the composition of the glass.

A simple but rather expensive process is to melt glass, cast a slab, roll the slab into a thickness close to the desired one, anneal, cut, grind and polish until the final dimensions are obtained.

All these methods require cutting and machining processes, which introduce surface flaws known as micro-cracks that lead to the reduction in the theoretical strength of glass sheets. If the cutting process is not conducted with care, additional warp can be introduced to the surface of the sheets due to the wobbling of the cutting blade.

1.4 Shaping Sheet Glass

Low-cost rectangular sheet glass is easy to obtain; however, the large surface warp of these optics necessitates the presence of at least one additional shaping process, where the surface warp is reduced to the required 0.5 μm tolerance. Some of the methods followed previously are presented.

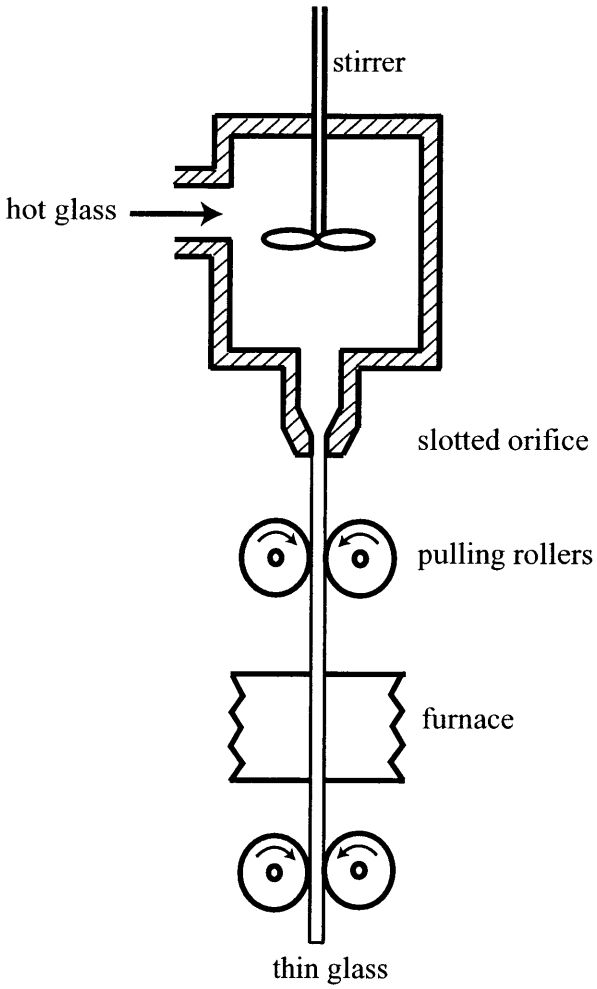

Figure 1-6: Manufacturing sheet glass using the slot-draw process

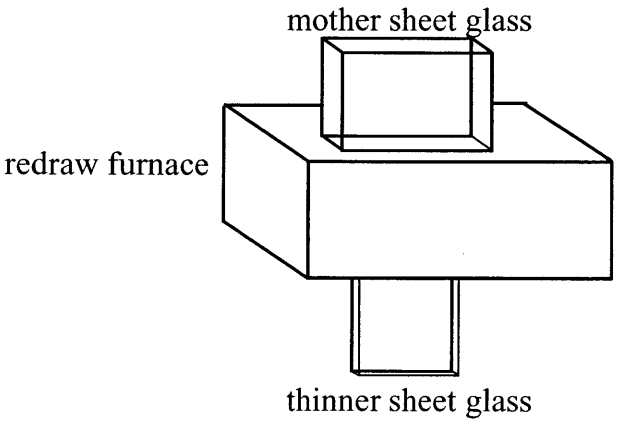

Figure 1-7: The redrawing process of a mother plate to obtain a thinner glass sheet

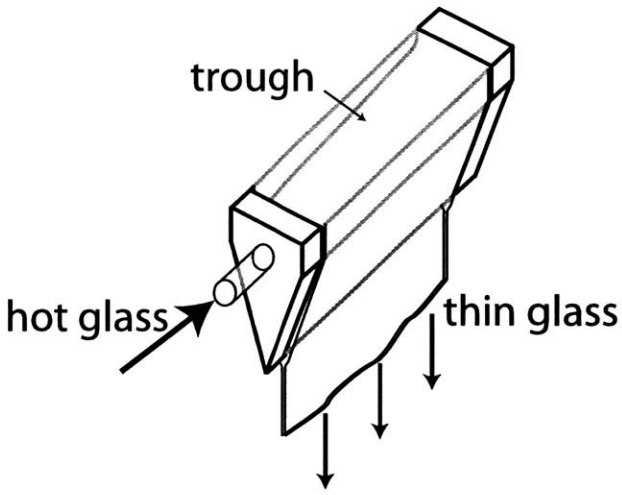

Figure 1-8: Fusion process, where glass flowing from a trough is reunited at the bottom of a V-shaped structure to form a thin sheet

1.4.1 Epoxy Replication

This process involves a very expensive mandrel, polished to the required surface smoothness and flatness, and an unpolished, thin substrate. The smooth surface of the mandrel is sputtered with gold. The thin substrate is to be placed on top of the gold layer; however, due to the difference between the substrate and mandrel surface topographies, a soft coating, such as epoxy, is sandwiched between the gold layer and the thin substrate, as shown in Figure 1-9. Epoxy is used to cover the mid-frequency errors of the thin substrate and reduce its RMS roughness. The substrate is pressed against the mandrel, and the epoxy is cured. The adhesion of gold to the mandrel is lower than that of gold to epoxy, making the process of detaching the substrate with the epoxy and gold from the mandrel tedious but possible. Ideally, the removed substrate would have replicated the smooth, flat surface of the mandrel; however, epoxy and the substrate have different coefficients of thermal expansion, which means that temperature variation causes a bi-material bending leading to a change in the overall surface warp of the substrate-epoxy-gold part. Other factors that must be taken into consideration are the shrinkage of epoxy as it cures, where curing is an exothermic reaction causing temperature fluctuations during the process,

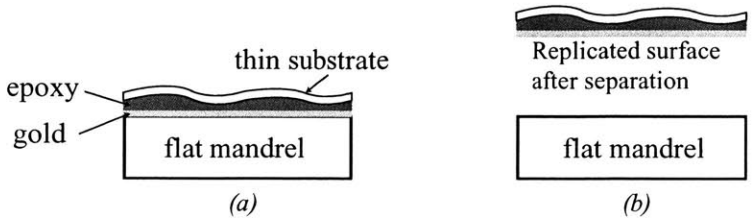

Figure 1-9: Epoxy replication of thin substrates, where *(a)* a master flat surface is sputtered with gold and a layer of epoxy is placed between the thin substrate and the gold layer to account for substrate flatness and roughness errors. After separation of the gold-epoxy-substrate *(b)* the gold surface ideally replicates the master surface.

and the purity of the epoxy layer while it is exposed to air and humidity; air bubbles trapped in the epoxy can cause protrusions in the gold layer. All these issues lead to the distortion of the optic's surface, rendering the final, accurate assembly process of all the mirrors an additional challenge [6].

1.4.2 Thermal Forming

Thermal shaping of glass has been around for centuries. The dependence of viscosity of glass on temperature was used to make vases and jewelry in Egypt and Syria. The discovery of fire-making allowed the development of arts based on fire, such as the firing of crude pottery, glaze, and glass. The process of thermal shaping has developed over the years from producing glass for decoration or general use to producing glass with micron accuracy [7]. Slumping is the thermal heating of glass until it sags under its own weight to take the shape of a precisely figured object it rests on. To better understand this process, significant temperature ranges that play an important role on the behavior of glass must be understood.

The *strain point* is the temperature at which annealing starts. It corresponds to a glass viscosity of $10^{14.5}$ poise.

The *annealing point* is the temperature at which annealing ends. At this point, internal strain in the glass is substantially eliminated. It corresponds to a glass

viscosity of 10^{13} poise.

The *softening point* is the temperature at which glass sags under its own weight. It corresponds to a glass viscosity of $10^{7.65}$ poise.

The *transformation temperature* or *glass temperature* T_g is the range in which glass transforms from its solid state to its plastic state. It corresponds to a glass viscosity of 10^{13} poise. It should be noted that the glass temperature is less than the annealing temperature by 5-50°C, depending on the material. In the transformation temperature region, glass must be cooled very slowly to release internal stress.

Additional thermal properties include the coefficient of thermal expansion and thermal conductivity of glass. Some of the important mechanical properties of glass include its density, Young's modulus, Poisson's ratio, and hardness. The tensile strength of glass is not taken into consideration because as described earlier, the true strength of glass depends on how crack-free the surface is. Tabulated data for the tensile strength of glass does not reflect its true strength. Tables 1.1 and 1.2 summarize the properties of different kinds of commercially available amorphous sheet glass that are potential candidates for X-ray optics. Temperature dependent properties such as Young's modulus and the coefficient of thermal expansion (CTE) are the values at room temperature. The coefficient of thermal expansion increases by $\sim 1 - 2{\times}10^{-6}/°\mathrm{C}$ as the temperature is increased above 300°C.

It is preferable to have a low density, high Young's modulus, low annealing and softening temperatures, and a threshold wavelength, which represents the wavelength at which the glass starts transmitting light, $>$ 300 nm because the metrology tool uses an arc lamp at 254 nm [30]. This prohibits reflection from the back surface of the optic that would introduce errors to the front surface measurement. The material of choice so far has been Schott D 263 glass for its availability in the form of rectangular sheets and its appealing properties. Ohara's L-BSL7 and L-BAL35, which are mostly available in circular shapes, are tempting candidates because of their properties; however, the price of one Ohara wafer is at least a hundred times that of Schott D 263, and since thousands of such wafers are needed eventually, price becomes a limiting factor. Ohara uses proprietary arsenic-free additives to decrease the critical

Glass brand	Density	Young's modulus	Torsion modulus	Poisson's	Knoop hardness
	g/cm^3	GPa	GPa	ratio	HK_{100}
Schott D 263	2.53	72.9	30.1	0.208	5.90
Schott AF 45	2.72	66	26.7	0.235	5.55
Ohara L-BSL7	2.38	79.3	32.7	0.214	5.60
Ohara S-BSL7	2.52	80	33.2	0.205	5.70
Ohara L-BAL35	2.82	100.8	40.3	0.252	6.30
Ohara S-LAL59	4.04	113.7	44	0.293	7.00
Corning 0211	2.53	74.45	30.31	0.22	4.58
Corning 7056	2.29	63	26.5	0.21	
Hoya SD-2	2.6	87	35	0.244	6.38

Table 1.1: Mechanical properties of different sheet glass brands

temperatures of the optics, and the circular optics are carefully cut and double-side polished to obtain an overall surface flatness of $\sim$5 μm and a total thickness variation (ttv) of < 1 μm compared to the < 600 μm flatness and ± 20 μm ttv of Schott rectangular sheets.

Slumping Steps

The process of thermal shaping does not affect the original microroughness and optic thickness variation. It only takes care of mid- to long-spatial wavelengths. The optic is placed in a furnace, and the temperature is elevated at a relatively high rate ($\sim 5 - 10$°C/min) until the strain temperature is reached. At this point, the temperature is held constant for a while to reduce thermal gradients in the bulk of the optic, which cause viscosity gradients and loss of control. Afterwards, the temperature is further increased at a lower rate ($\sim 1 - 2$°C/min) to a temperature between the softening and annealing points (around 620°C), to allow for the stress relieved glass to slowly deform under its own weight without changing the thickness uniformity. The glass at this point takes the shape of the object it rests on. The longer the glass is left at this temperature, the better it will replicate the master surface. Once the

Glass brand	Strain temp. °C	Annealing temp. °C	Softening temp. °C	CTE $10^{-6}/°C$	Thermal conductivity W/mK	Wavelength threshold nm
Schott D 263	529	557	736	6.3		329
Schott AF 45	627	663	883	4.5		315
Ohara L-BSL7	464	448	630	5.8	1.169	280
Ohara S-BSL7	532	563	718	7.2	1.130	280
Ohara L-BAL35	489	520	619	6.6	1.126	290
Ohara S-LAL59	591	620	696	5.5	0.863	270
Corning 0211	508	550	720	7.38		
Corning 7056	472	512	718	5.15		
Hoya SD-2	669	720	787	3.2		<250

Table 1.2: Thermal and optical properties of different sheet glass brands

replication process is complete, the temperature of the glass is slowly reduced until the strain point is reached once again. The slow rate of cooling reduces the initiation of internal stresses. After the strain temperature is held for a while, the glass can be cooled at a faster rate. Figure 1-10 summarizes the temperature curve followed for a typical slumping process.

Various groups have followed this temperature profile utilizing different mechanisms to thermally shape glass. Slumping onto precision mandrels has been the most prominent approach, where an expensive, smooth mandrel figured to the desired shape is used as a master, on which the thin optic is placed. The assembly is put in a furnace, and the slumping temperature profile is followed. Several problems have been observed. The presence of dust particles between the mandrel and the thin optic leads to high spatial frequency errors in the form of dimples. It has been noted that careful cleaning of both mandrel and glass, in an attempt to get rid of dust particles, leads to catastrophic results. Since slumping requires elevated temperatures, the glass fuses to the mandrel. A difference in the coefficient of thermal expansion between the thin glass and the mandrel could lead to the shattering of the

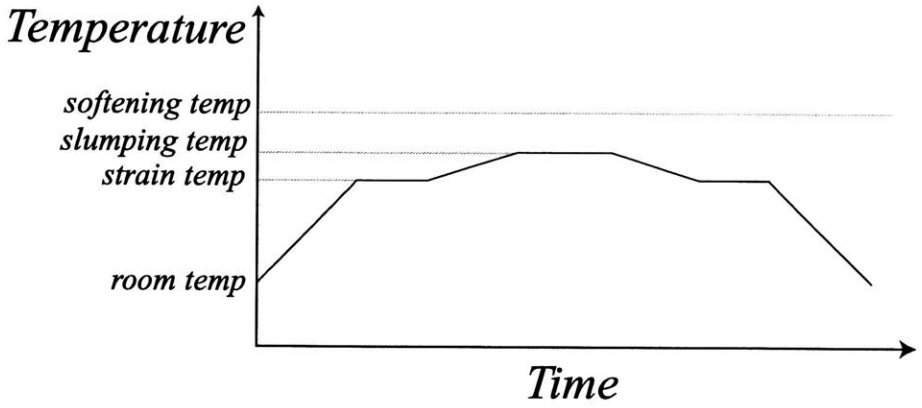

Figure 1-10: Temperature profile followed to slump thin glass optics

glass upon cooling and damaging the polished surface of the mandrel. Dust particles are of random size and distribution. A secondary step involving epoxy replication has been used in an attempt to fill in the dimples left by dust particles. This step introduces all the problems associated with epoxy discussed earlier. Another solution is the use of anti-stick coating usually found in the form of powder, which can stand high temperatures. Applying a layer of powder with a uniform thickness between the mandrel and the thin optic is a demanding task.

This process can be performed using either a flat mandrel or a cylindrical one that provides conical optics used for the mirrors in the Wolter I configuration, as shown in Figure 1-11.

In an attempt to reduce the effects of dust particles, slumping to pin chucks was investigated at the *Space Nanotechnology Laboratory.* An array of thousands of $25 \times 25 \times 2.5$ μm^3 fused silica pins separated by a distance of 0.25 mm were fabricated on a flat mandrel, as shown in Figure 1-12, to decrease the surface area in contact with the mandrel and the probablility of having dust particles trapped between the pins and glass. These particles tend to settle in the spaces between the pin chucks. The pins are coated with a thin, rough layer of TiO_2 to avoid the optic from sticking to the pins and damaging them. Although this method proved to be successful for small glass sheets, the process of coating a rough TiO_2 layer on the pins has not been

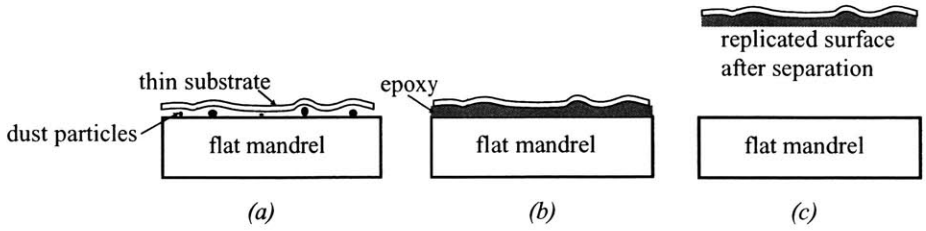

Figure 1-11: Slumping thin optics on flat mandrels with epoxy replication. *(a)* shows slumping of a thin optic on a flat mandrel with the presence of dust particles that cause mid- to high-frequency errors. *(b)* shows a second step where epoxy is used to fill in the dimples left by the dust particles, and *(c)* shows the ideal case where the epoxy layer would have replicated the surface of the mandrel with high fidelity.

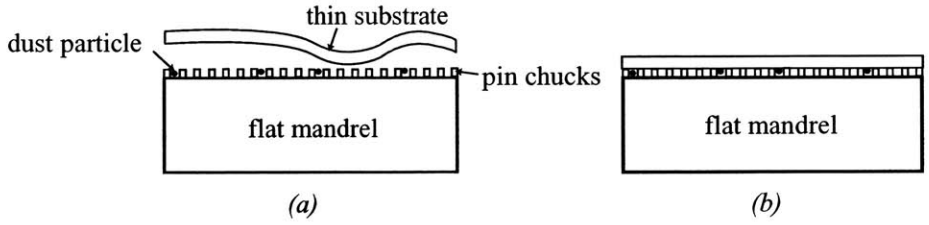

Figure 1-12: An array of pins fabricated on a flat fused silica mandrel to allow for dust particles to settle between pins. *(a)* shows a thin substrate at room temperature and *(b)* shows the substrate after slumping.

reproducible, and similar results have not been achieved on larger optics of interest. Bonding between the optic and the pins remains a major problem [9].

A third method utilizes a semi-cylindrical quartz shell mandrel, where the thin optic is placed on the concave side of the shell, as shown in Figure 1-13. The optic is cut to a length equal to the diameter of the cylinder. As the temperature is increased, the optic sags to theoretically take the shape of the cylinder; however, the accuracy of the final shape depends on the presence of obstacles, the slopes on the inner surface of the concave shell, and the edges of the thin optic. If conducted properly, this process prevents the critical surface of the optic from coming in contact with any other surface. The temperature at which the optic sags can not be maintained for

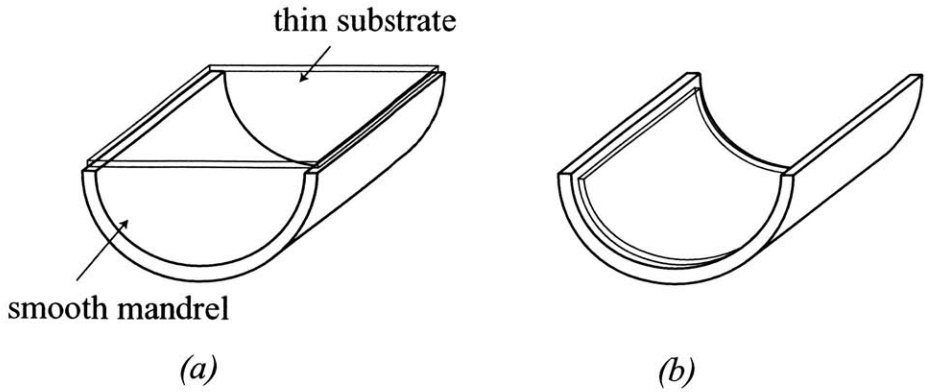

Figure 1-13: Slumping thin glass substrates on smooth, semi-cylindrical mandrels. *(a)* shows the substrate resting on the mandrel at room temperature, and *(b)* shows the substrate conforming to the shape of the mandrel as the temperature is increased.

a long time to avoid contact between the optic and the mandrel as the optic sags. Any temperature gradient along the optic during this short period of time causes a non-uniform sag, distorting the final surface [6].

A novel approach is investigated to reduce problems associated with sticking, where the optic is carried by a layer of air evenly distributed along the area of the optic using a porous ceramic.

1.5 Thermal Forming Using Porous Ceramics

Porous compensation has replaced orifice compensation in air bearings used to carry heavy loads for several reasons, the most prominent being the fact that porous bearings provide a more uniform pressure distribution, as shown in Figure 1-14. The pressure drop along the porous compensation is less than that along the orifice one. These factors lead to a higher load capacity, better stiffness, and better tilt resistance.

Porous bearings are usually made of ceramic materials such as alumina and silicon carbide, even though graphite and metal bearings are common as well. Ceramics are a better candidate for air bearings for various reasons: they do not corrode in any fluid environment that might be used during their manufacturing, they are brittle,

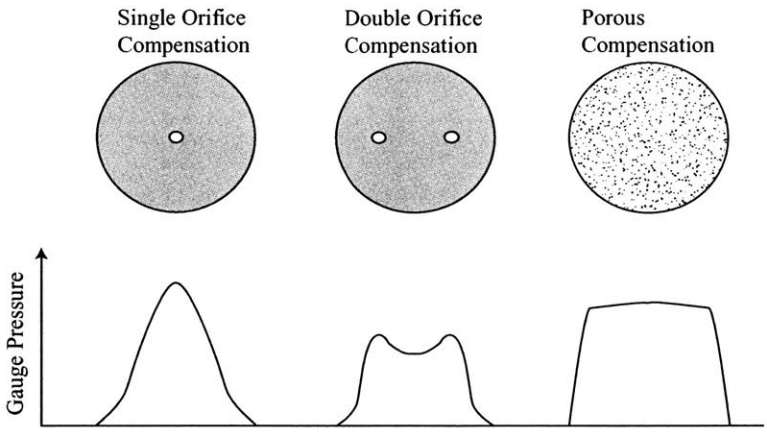

Figure 1-14: Pressure distribution of air bearings with different types of compensation. Both single and double orifice compensation methods have large pressure gradients, whereas porous compensation provides an almost uniform pressure distribution over most of the bearing area [10].

which means minimum plastic deformation is generated during grinding and lapping, leading to a surface with a negative skewness and minimal residual stress, their surface finish is limited by the size of the grain used in sintering, they have a high Young's modulus with a low density, they have high dimensional stability, and they do not brinell because of their high allowable Hertz stress [11]. These features are critical in air bearings, where the air gap between the bearing and the carried load is on the order of 10 μm, and any damage to the surface leading to air gap variation deteriorates the overall performance of the bearing.

Preliminary experiments have been conducted at the *Space Nanotechnology Laboratory* using porous bearings with a surface flatness of less than a micron and millions of pores for slumping thin optics. The thin layer of air between the bearing and the optic is large enough to accommodate dust particles and reduce their effect on the optic. The air gap prohibits contact between the optic and any other surface, eliminating the sticking problem observed before. This allows for the slumping process to be conducted at longer periods of time, permitting the optic to better replicate the master surface.

Although the pressure distribution of a porous bearing is more uniform than other forms of compensation, a pressure gradient still exists in the film. The pressure at the center of the bearing is close to the supply one, whereas the pressure at the edge is atmospheric. This pressure gradient imprints itself on the optic as it softens. This effect has been seen on a rectangular glass sheet with a pressure gradient at its bottom surface and constant atmospheric pressure at the top surface. The glass has a dome shape after the slumping process is completed.

Placing an air bearing on both sides of the optic has been investigated in order to have the same pressure gradient on both sides. The force exerted by the air bearing on the optic depends on the air gap thickness, as shown in Figure 1-15. Maintaining an equal gap on both sides of an optic that has a starting flatness greater than 100 μm is a challenge, and this leads to unequal forces on both sides of the optic.

A third approach using porous ceramics constitutes the theme of this thesis. To reduce the pressure gradient in the air film, sub-millimeter grooves are machined on the top surface of the ceramic to allow for the air to leak out to the atmosphere without building pressure up at the center of the ceramic part. This method does not use the typical air bearing theories. The pressure in the gap is close to atmospheric and not the supply pressure.

The second chapter describes the theory behind the performance of porous materials as air bearings. Numerical analysis is used to model the flow in porous bearings to predict the pressure profile in the air gap between the bearing and the sheet glass or carried load.

The third chapter explains some of the important mechanical properties of materials, and how these properties are affected by porosity and temperature elevation. It also describes the process of shaping thin glass optics using porous materials as the flat master.

The fourth chapter discusses a novel method for constraining thin optics with minimal deformation to measure their true surface topography.

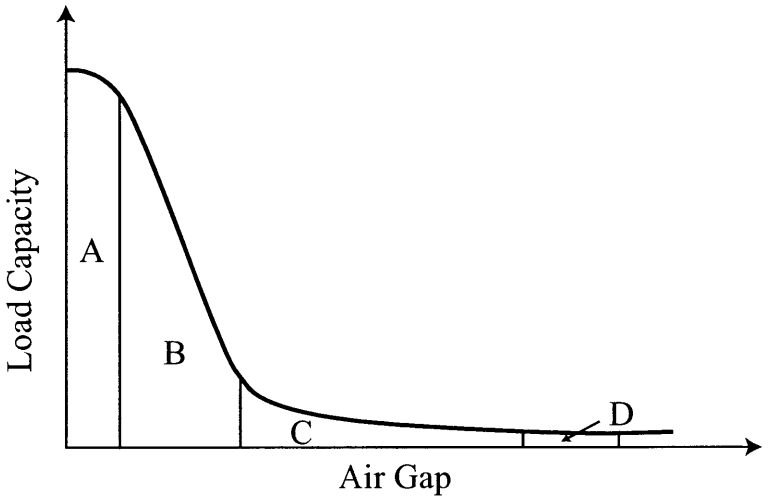

Figure 1-15: Ideal load capacity of an air bearing versus air gap thickness. Region A is usually between 0 and 5 μm, where the stiffness of the air film (slope of the curve) changes with a slight variation in gap thickness. Region B is the operational region usually ranging between 5 and 15 μm, where ideally the stiffness does not change significantly with gap variation. In region C, the flow of air may go into the supersonic regime, and the load capacity becomes negative (not shown in this figure), meaning that the bearing attracts the load towards it rather than pushing it away. Region D is when the forces are jet impact forces and not viscous ones as before.

Chapter 2

Flow in Porous, Rectangular Ceramics

Air bearings utilize fully developed boundary layers in a thin film between two surfaces, with a film pressure higher than atmospheric, to provide the bearing with load carrying abilities. Porous bearings have been recently used more often than conventional restrictors due to their ease of manufacturing, higher load capacity, better stiffness and superior damping characteristics. Porosity of a solid determines its capacity to store fluids. Air at certain supply pressure is transported through the connected pores, where the rate of transport depends on the interaction between the fluid and the porous channels. Gases display a permeability that not only depends on the porous medium as in the case of liquids, but also on the identity of the gas and the pressure differential across the medium. This dependence is known as slippage and becomes more significant as the pore diameters approach the mean free path of the gas molecule.

2.1 Flow Through Porous Media

Most studies in characterizing single-phase fluid flow in porous media use Darcy's law, which states that the velocity of a fluid V in a given direction is proportional to the pressure difference ΔP along that direction and inversely proportional to the

length of the specimen L. The permeability factor k and the viscosity of the fluid μ determine the coefficient of proportionality

$$V = -\frac{k}{\mu}\frac{\Delta P}{L}. \tag{2.1}$$

This model is only valid for viscous, creeping flow with low values of Reynolds number [12]

$$Re = \frac{\rho V d_p}{\mu}, \tag{2.2}$$

where ρ is the fluid density and d_p is the grain diameter. The porous medium must not be reactive with the flowing fluid, and there should be no fluid accumulation. The effects of fluid inertia have been investigated; inertial fluid mostly results from the loss of momentum as the fluid expands and contracts, twists and turns within the inter-connected pores at high local fluid velocity. The most widely accepted model that describes the effects of inertial flow is the Forchheimer's equation, which adds a second order velocity term to Darcy's equation

$$-\frac{\Delta P}{L} = \frac{\mu}{k_1}V + \frac{\rho}{k_2}V^2, \tag{2.3}$$

where k_1 and k_2 are the Darcian (viscous) and non-Darcian (inertial) permeabilities, respectively.

Several experiments have been conducted to prove that the Forchheimer model is not valid at low flow velocities, and that Darcy's model provides a better fit to experimental data [13]. It has also been shown that aerostatic bearings follow a low-flow regime, justifying the use of Darcy's equation.

2.2 Temperature Increase Effects

As the temperature of air, a perfect gas, increases from room temperature to around 650°C, intermolecular forces are still negligible, and the change in density can be calculated using the perfect gas law

	20°C	650°C	% change
Density (kg/m^3)	1.2	0.39	-67.5
Viscosity (μPa.s)	18.3	42	130

Table 2.1: Properties of air at room and working temperatures

$$\rho = \frac{P}{RT}, \tag{2.4}$$

where ρ is the gas density, P is the given pressure in Pa, R is the universal constant and equals 284 J/kg.K, and T is the absolute temperature. In order to estimate the change in viscosity of air due to temperature elevation, the Sutherland equation is used

$$\frac{\mu}{\mu_o} = \left(\frac{T}{T_o}\right)^{\frac{1}{2}} \frac{1+\frac{S}{T_o}}{1+\frac{\frac{S}{T_o}}{\frac{T}{T_o}}}, \tag{2.5}$$

where μ is the viscosity at absolute temperature T, μ_o is the viscosity at room temperature T_o and equals 1.83×10^{-5} Pa.s, and the ratio $\frac{S}{T_o}$ is empirically taken as 0.505 [14]. Table 2.1 summarizes the properties of air at both room temperature and at 650°C.

The permeability k used in Darcy's equation is an intrinsic material property independent of the fluid used to measure it; therefore, a change in viscosity (different fluid) does not directly affect the permeability of the porous material. The temperature dependence of permeability in porous media is rarely stated explicitly in literature; however, experiments show that permeability decreases with increasing temperature. Innocentini et al. [15] evaluated the air-flow permeability of refractory castables at temperatures up to 800°C. They show that both Darcian and inertial permeabilities decrease as the temperature of both gas and porous medium increases. Recrystallization and grain growth are associated with elevated temperatures, where a new set of strain-free grains form with an increase in average grain size, followed by grain boundary motion. This leads to smaller clearances or pore sizes between grains, which in turn may lead to a reduction in the overall permeability of the ceramics.

2.3 Theoretical Analysis of Flow in Rectangular Porous Aerostatic Bearings

As the thin glass optic temperature is raised, its viscosity decreases and the optic sags under its own weight. Since the optic is supported by a thin layer of air, it is important to study the air pressure distribution in the small gap between the optic and the bearing surface because the optic will replicate this distribution while it is soft.

2.3.1 Preliminary Assumptions

Several assumptions are made and followed throughout the analysis of flow in different bearing configurations. The flow in the porous bearing is characterized by Darcy's law from Equation 2.1, the permeability coefficients along x, y, and z directions are constant, the gas follows perfect (ideal) gas laws and is isothermal through the bearing, steady state conditions prevail, the pressure gradient along the z direction in the gap is negligible compared to the pressure gradient along the x and y directions, where the flow is laminar, there is no fluid accumulation in the porous medium, there is no slip at the optic plane boundary, which means that the air velocity at the optic interface is zero; however, slip occurs at the porous bearing boundary, where the velocity vector U in the air gap is the same as the average velocity vector U' in the porous bearing at the surface [16].

2.3.2 Boundary Conditions

The porous bearing is sealed on all side surfaces; therefore, there is no pressure gradient across these edges. The bottom surface is at the supply pressure P_s. The top surface perimeter is at atmospheric pressure. The final boundary condition is at the interface between the top surface and the small air gap [17]. Neglecting body forces and inertial terms, the Navier Stokes equation for the flow in the air gap reduces to

$$\frac{\partial^2 U}{\partial z^2} = \frac{1}{\mu}\nabla p, \tag{2.6}$$

where U is the velocity in the air gap, z is the vertical direction, μ is the viscosity of the fluid, and p is the pressure of the fluid, which has been assumed to be equal to the pressure at the porous bearing top surface.

Integrating Equation 2.6 twice with boundary conditions $U = U'$ at $z = 0$ and $U = 0$ at $z = h$, where h is the air gap thickness, the velocity distribution is

$$U = \frac{1}{2\mu} z \Big(z - h \Big) \nabla p + \frac{h - z}{h} U'. \tag{2.7}$$

The continuity equation in the air gap is

$$\frac{\partial u}{\partial x} + \frac{\partial v}{\partial y} + \frac{\partial w}{\partial z} = 0, \tag{2.8}$$

where u, v, and w are the velocity components along the x, y, and z directions respectively. Substituting Darcy's law from Equation 2.1 with $V = U'$ for this case and Equation 2.7 into Equation 2.8, and integrating it with respect to z from $z = 0$ to $z = h$, the modified Reynold's equation is obtained

$$\frac{\partial}{\partial x}\left[h(h^2 + 6k_x)\frac{\partial p}{\partial x}\right] + \frac{\partial}{\partial y}\left[h(h^2 + 6k_y)\frac{\partial p}{\partial y}\right] = 12k_z \left(\frac{\partial p'}{\partial z}\right)_{z=H}, \tag{2.9}$$

where h is the air gap thickness, p is the pressure in the air gap, p' is the pressure in the porous medium, H is the thickness of the porous bearing and k_x, k_y, and k_z are the permeabilities along the x, y, and z directions, respectively.

2.3.3 Theoretical Analysis of Flow in Flat Bearings

This model accounts for the pressure distribution between the flat bearing and the thin optic. The equation governing the flow in the porous medium can be obtained by combining Equations 2.1 and 2.8, such that

$$k_x \frac{\partial^2 p'}{\partial x^2} + k_y \frac{\partial^2 p'}{\partial y^2} + k_z \frac{\partial^2 p'}{\partial z^2} = 0. \tag{2.10}$$

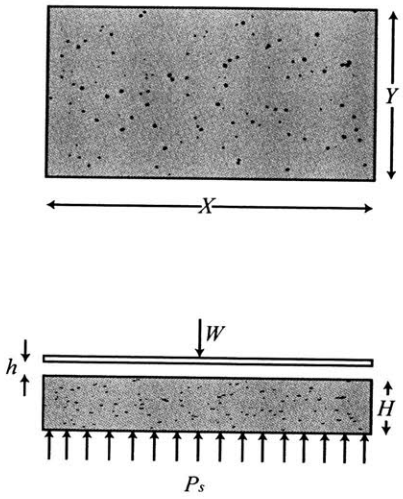

Figure 2-1: Porous bearing dimensions.

For a porous medium of length X, width Y and thickness H, as shown in Figure 2-1, a non-dimensional form of Equations 2.9 and 2.10 can be formed by substituting $\tilde{x} = x/X$, $\tilde{y} = y/Y$, $\tilde{z} = z/H$, $\tilde{p} = p/p_a$, and $\tilde{p'} = p'/p_a$, such that

$$a\frac{\partial^2 \tilde{p}}{\partial \tilde{x}^2} + b\left(\frac{X}{Y}\right)^2 \frac{\partial^2 \tilde{p}}{\partial \tilde{y}^2} = \left(\frac{\partial \tilde{p'}}{\partial \tilde{z}}\right)_{\tilde{z}=1} \tag{2.11}$$

$$K_x \frac{\partial^2 \tilde{p'}}{\partial \tilde{x}^2} + K_y \left(\frac{X}{Y}\right)^2 \frac{\partial^2 \tilde{p'}}{\partial \tilde{y}^2} + \left(\frac{X}{H}\right)^2 \frac{\partial^2 \tilde{p'}}{\partial \tilde{z}^2} = 0, \tag{2.12}$$

where $K_x = k_x/k_z$, $K_y = k_y/k_z$, $a = 1/\Lambda + 1/2K_x(Hh/X^2)$, $b = 1/\Lambda + 1/2K_y(Hh/X^2)$, and $\Lambda = 12k_z X^2/h^3 H$.

Numerical Solution of Governing Equations

Equations 2.11 and 2.12 can be solved using the elliptic equations of the finite difference method [18]. Figure 2-2 shows a three-dimensional grid used for the finite-difference solution of elliptic partial differential equations in three independent variables. The central differences based on this grid scheme are

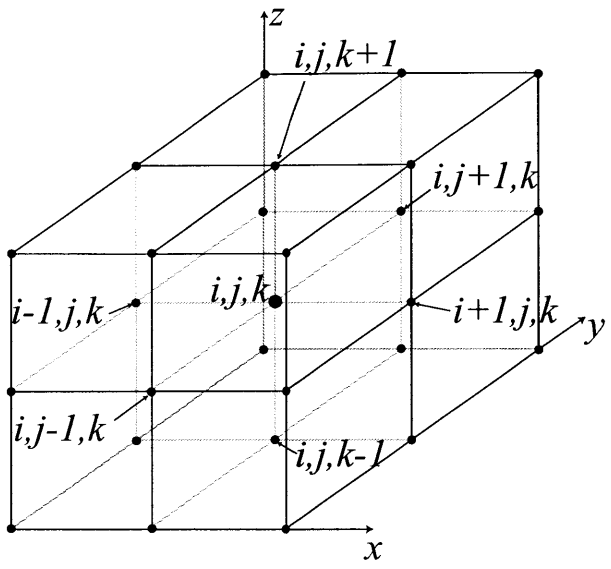

Figure 2-2: A grid used for the finite-difference solution of elliptic partial differential equations in three independent variables.

$$\frac{\partial^2 \tilde{p'}}{\partial \tilde{x}^2} = \frac{\tilde{p'}_{i+1,j,k} - 2\tilde{p'}_{i,j,k} + \tilde{p'}_{i-1,j,k}}{\Delta \tilde{x}^2} \tag{2.13}$$

$$\frac{\partial^2 \tilde{p'}}{\partial \tilde{y}^2} = \frac{\tilde{p'}_{i,j+1,k} - 2\tilde{p'}_{i,j,k} + \tilde{p'}_{i,j-1,k}}{\Delta \tilde{y}^2} \tag{2.14}$$

$$\frac{\partial^2 \tilde{p'}}{\partial \tilde{z}^2} = \frac{\tilde{p'}_{i,j,k+1} - 2\tilde{p'}_{i,j,k} + \tilde{p'}_{i,j,k-1}}{\Delta \tilde{z}^2}, \tag{2.15}$$

where $\Delta\tilde{x}$, $\Delta\tilde{y}$, and $\Delta\tilde{z}$ represent the grid dimensions.

The first order derivative in Equation 2.11 can be solved using the centered finite-divided-difference formula represented by

$$\frac{\partial \tilde{p'}}{\partial \tilde{z}} = \frac{\tilde{p'}_{i,j,k+1} + \tilde{p'}_{i,j,k-1}}{2\Delta \tilde{z}}. \tag{2.16}$$

Replacing Equations 2.13 through 2.16 into Equations 2.11 and 2.12, while $\Delta\tilde{x} = \Delta\tilde{y} = \Delta\tilde{z} = \Delta$, the pressure at every node in the porous medium can be obtained by using

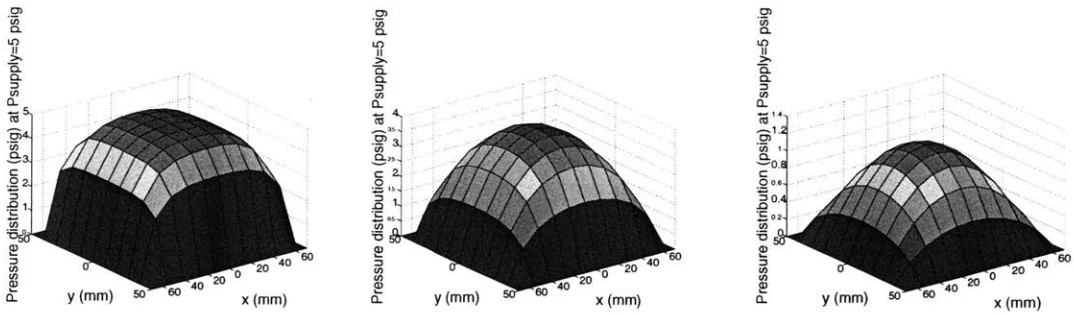

Figure 2-3: The pressure profile in the air gap of a 140 mm×100 mm×12.7 mm porous bearing at film thickness of *(a)* 5 μm, *(b)* 10 μm, and *(c)* 20 μm.

$$\tilde{p}_{i,j,kH} = \frac{a(\tilde{p}_{i+1,j,kH} + \tilde{p}_{i-1,j,kH}) + b(X/Y)^2(\tilde{p}_{i,j+1,kH} + \tilde{p}_{i,j-1,kH}) - \Delta/2(\tilde{p}_{i,j,kH+1} + \tilde{p}_{i,j,kH-1})}{2a + 2b(X/Y)^2} \tag{2.17}$$

$$\tilde{p}_{i,j,k} = \frac{K_x(\tilde{p}_{i+1,j,k} + \tilde{p}_{i-1,j,k}) + K_y(X/Y)^2(\tilde{p}_{i,j+1,k} + \tilde{p}_{i,j-1,k}) + (X/H)^2(\tilde{p}_{i,j,k+1} + \tilde{p}_{i,j,k-1})}{2\left(K_x + K_y(X/Y)^2 + (X/H)^2\right)}. \tag{2.18}$$

It should be noted that $\tilde{p}_{i,j,kH+1}$ is the same as $\tilde{p}_{i,j,kH}$, where $\tilde{p}_{i,j,kH}$ is the pressure at $\tilde{z} = 1$, since it has been assumed that the pressure drop in the air gap along the z direction is negligible.

To plot the pressure distribution in the air gap, Equations 2.17 and 2.18 are iterated with the boundary conditions set before and the dimensions of $X = 140$ mm, $Y = 100$ mm, and $H = 12.7$ mm. The permeability of the isotropic alumina part used is the same in all directions and equals 10^{-14} m^2 at room temperature. Following the rate of decrease in permeability shown by Innocentini et al. for a porous bearing fired at temperatures greater than 1500°C, the effective permeability is 5×10^{-15} m^2. Figure 2-3 shows this pressure profile for a supply pressure of $P_s = 5$ Psig and different values of air gap thickness h.

The load capacity W of this bearing defined as the maximum load a bearing can carry as the air gap approaches zero at a supply pressure of $P_s = 5$ Psig is found to

be 319 N using

$$W = \int_0^X \int_0^Y (p - p_a) dx dy. \tag{2.19}$$

As the air gap thickness increases, the pressure drop is more dramatic and the profile changes from an almost flat distribution to a dome-shape. The weight of the optics of interest being less than 0.14 N, the smallest feasible pressure on the large bearing area results in a force that lifts the optic by tens of microns. Experiment shows the drastic effects of pressure drop at large air gaps on the topography of the optic, which follows the pressure distribution in the relatively large gap.

2.3.4 Theoretical Analysis of Flow in Grooved Bearings

In an attempt to eliminate the large pressure gradient in the air gap, the machining of grooves onto the top surface of the porous medium has been considered. The role of these grooves is to allow for a passage for the air at the center of the bearing to leak out into the atmosphere, thus decreasing the resistance of the path from the center to the edges of the bearing. In this lay out, the porous medium does not act as a typical air bearing, where the fully developed boundary layer supports the load, but rather the load is supported by the combination of inertial (jet impact) and viscous forces of individual flat lands. The ceramic is coated with a thin layer of alumina to plug the valleys and side walls of the grooves, and the top surface is later lapped to remove the coating from the peak regions. This forces the air to leave the porous ceramic through the peak regions, thus lifting the optic and escaping to the atmosphere through the plugged grooves, as shown in Figure 2-4.

The equation for the flow inside the porous medium is the same as before except at the nodes surrounding the grooves, where the width and depth of the plugged grooves must be taken into consideration. The finite difference method is replaced by the control volume approach, which offers an alternative way to numerically approximate partial differential equations (PDEs). This is especially useful for cases with irregularly shaped boundaries or more complex geometries. This approach re-

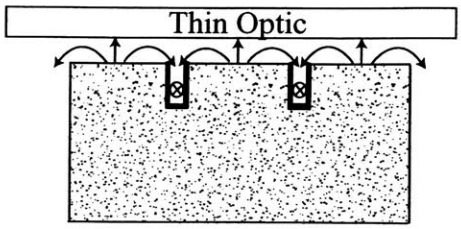

Figure 2-4: Air leaving porous ceramic through the peak regions to lift the optic, fill the plugged grooves and escape to the atmosphere without building up a large pressure gradient.

sembles the point-wise approach in that points are determined across the domain. However, rather than approximating the PDE at a point, the approximation is applied to a volume surrounding the point. This volume is formed by the perpendicular lines through the midpoint of each line joining adjacent nodes. Figure 2-5 shows the difference between the finite-difference and control volume approaches.

In order to establish the equations for the nodes surrounding the plugged grooves, consider Figure 2-6, which shows the control volumes around a single groove along the y direction.

For the control volume of the node beneath the groove, the sum of flow rates in all directions must be zero, since it has been assumed that there is no fluid accumulation in the porous medium. The flow rate Q is given by

$$Q = U'A, \tag{2.20}$$

where U' is the velocity in the porous medium governed by Darcy's law from Equation 2.1, and A is the area of the control volume edge surfaces. Note that A is the product of the lengths of the edges along all surfaces except at the surface where the groove is located, in this case the top surface, where A is $(1 - delx)\Delta x\Delta y$ with $delx = g_{wx}/\Delta x$, and g_{wx} is the width of the plugged groove that does not allow for flow to go through the boundary. The sum of flow rates along the edges of the control volume is

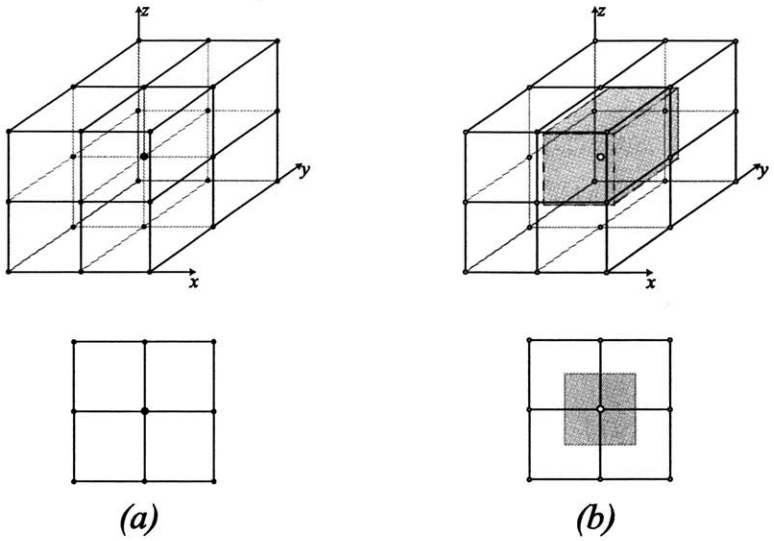

Figure 2-5: 3-D schematic and 2-D projection of two different methods for developing approximate solutions for partial differential equations: (a) finite-difference and (b) control volume.

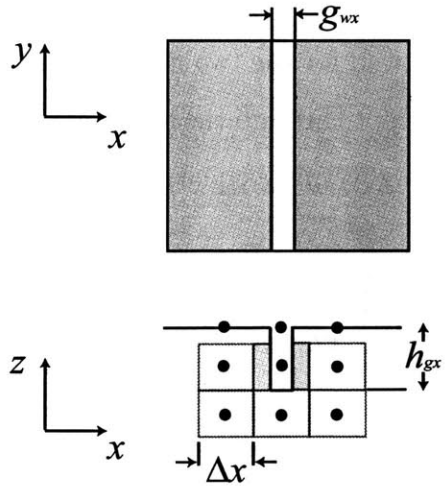

Figure 2-6: Nodes surrounding a plugged groove along the y direction.

$$\sum Q = U'_{x1}\Delta y\Delta z + U'_{x2}\Delta y\Delta z + U'_{y1}\Delta x\Delta z + U'_{y2}\Delta x\Delta z + U'_{z1}\Delta x\Delta y + U'_{z2}(1-delx)\Delta x\Delta y = 0, \tag{2.21}$$

where the x, y, and z subscripts represent the direction involved, and the 1 and 2 subscripts represent both sides of a single direction. Replacing velocity with pressure from Darcy's law from Equation 2.1, non-dimensionalizing, and writing the pressure using the i, j, and k subscripts the following equation is obtained

$$\tilde{p}_{i,j,k} = \frac{K_x(\tilde{p}_{i+1,j,k} + \tilde{p}_{i-1,j,k}) + K_y(X/Y)^2(\tilde{p}_{i,j+1,k} + \tilde{p}_{i,j-1,k}) + (X/H)^2(\tilde{p}_{i,j,k+1}(1 - delx) + \tilde{p}_{i,j,k-1})}{2\left(K_x + K_y(X/Y)^2 + \frac{(X/H)^2}{2}(1 + (1 - delx))\right)} \tag{2.22}$$

If grooves in the x direction are added such that $dely = g_{wy}/\Delta Y$, where g_{wy} is the width of the groove along the x direction, then by following similar steps, it can be shown that Equation 2.22 becomes

$$\tilde{p}_{i,j,k} = \frac{K_x(\tilde{p}_{i+1,j,k} + \tilde{p}_{i-1,j,k}) + K_y(X/Y)^2(\tilde{p}_{i,j+1,k} + \tilde{p}_{i,j-1,k}) + (X/H)^2(\tilde{p}_{i,j,k+1}C + \tilde{p}_{i,j,k-1})}{2\left(K_x + K_y(X/Y)^2 + \frac{(X/H)^2}{2}(1 + C)\right)}, \tag{2.23}$$

where $C = (1 - delx)(1 - dely)$.

The same procedure is followed for the two nodes on each side of the groove, where flow can go in all directions except through the side edges. For a bearing with grooves along the y direction only, the governing equation is

$$\tilde{p}_{i,j,k} = \frac{K_x\tilde{p}_{i\pm1,j,k} + K_y(X/Y)^2(\tilde{p}_{i,j+1,k} + \tilde{p}_{i,j-1,k}) + (X/H)^2(\tilde{p}_{i,j,k+1} + \tilde{p}_{i,j,k-1})}{2\left(K_x/2 + K_y(X/Y)^2 + (X/H)^2\right)}. \tag{2.24}$$

If the grid is such that every one of these nodes lies between two grooves as shown in Figure 2-7, then Equation 2.24 reduces to

$$\tilde{p}_{i,j,k} = \frac{K_y(X/Y)^2(\tilde{p}_{i,j+1,k} + \tilde{p}_{i,j-1,k}) + (X/H)^2(\tilde{p}_{i,j,k+1} + \tilde{p}_{i,j,k-1})}{2\left(K_y(X/Y)^2 + (X/H)^2\right)}. \tag{2.25}$$

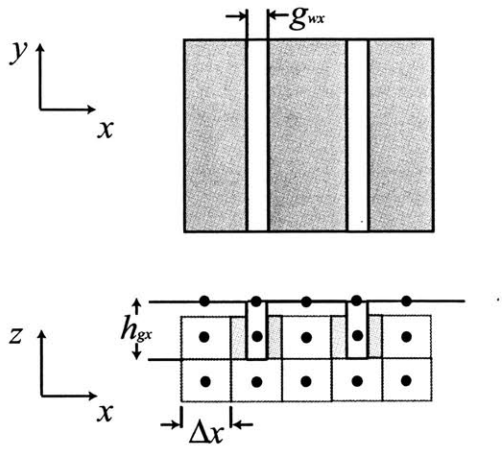

Figure 2-7: Nodes surrounding two plugged grooves along the y direction.

The equation for the nodes at the surface of the porous medium previously governed by the modified Reynold's Equation must be changed to account for the presence of the grooves as well. The validity of this equation depends on the depth of the grooves. For shallow grooves, laminar flow dominates and a slight modification of Equation 2.9 would be sufficient; however, as the groove depth increases, inertial effects become more important, and a more complicated solution of the Navier-Stokes equation, considering both inertial and viscous flows, would be required.

The analysis that follows is for shallow grooves, where the flow can still be assumed to be viscous laminar. Figure 2-8 shows the geometry of a single grid $\Delta X \times \Delta Y$ at the top surface of the porous medium with a groove of width g_{wx} at its center. $1 - \frac{g_{wx}}{\Delta X}$ of the land has the original air gap of h, whereas $\frac{g_{wx}}{\Delta X}$ has an air gap of $h + h_{gx}$, where h_{gx} is the depth of the groove. A similar analogy can be made for grooves g_{wy} wide and h_{gy} deep in the y direction. Therefore, replacing the original air gap h with this gap variation [19], Equation 2.17 for a bearing with grooves in both x and y directions can be rewritten as

$$\tilde{p}_{i,j,kH} = \frac{t(\tilde{p}_{i+1,j,kH} + \tilde{p}_{i-1,j,kH}) + o(\tilde{p}_{i,j+1,kH} + \tilde{p}_{i,j-1,kH}) - \frac{\Delta}{2}\tilde{p}_{i,j,kH-1}}{2t + 2o + \frac{\Delta}{2}}, \qquad (2.26)$$

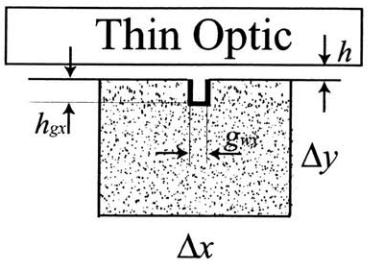

Figure 2-8: A single groove of width g_{wx} and height h_{gx} in one grid area $\Delta X \times \Delta Y$. The groove side walls and base are coated to avoid air from leaking out before it can actually lift the optic.

where

$$t = \frac{H}{12k_z X^2}\left((1-dely)h^3 + dely(h+h_{gy})^3\right) + \frac{HK_x}{2X^2}\left((1-dely)h + dely(h+h_{gy})\right) \tag{2.27}$$

$$o = \frac{H}{12k_z X^2}\left(\frac{X}{Y}\right)^2\left((1-delx)h^3 + delx(h+h_{gx})^3\right) + \frac{HK_y}{2X^2}\left(\frac{X}{Y}\right)^2\left((1-delx)h + delx(h+h_{gx})\right). \tag{2.28}$$

Using Equations 2.18, 2.23, 2.24, and 2.26 with the boundary conditions stated previously, the pressure distribution of a grooved bearing can be modeled. Figure 2-9 shows the pressure distribution of a 5×5 mm^2 porous bearing with one groove at an air gap of 5 μm. The pressure at the center of the bearing, where the groove is located, is very close to atmospheric. A slight pressure builds up at the peaks; however, the pressure gradient between the peaks and valleys is <0.12 Psig. As the gap gets larger, the pressure gradient drops significantly. The larger ceramic part is a network of such small islands of peaks and valleys, where every groove will contribute to allowing the air in the film to leak out and remain at a pressure close to atmospheric, thus reducing pressure gradients throughout the film.

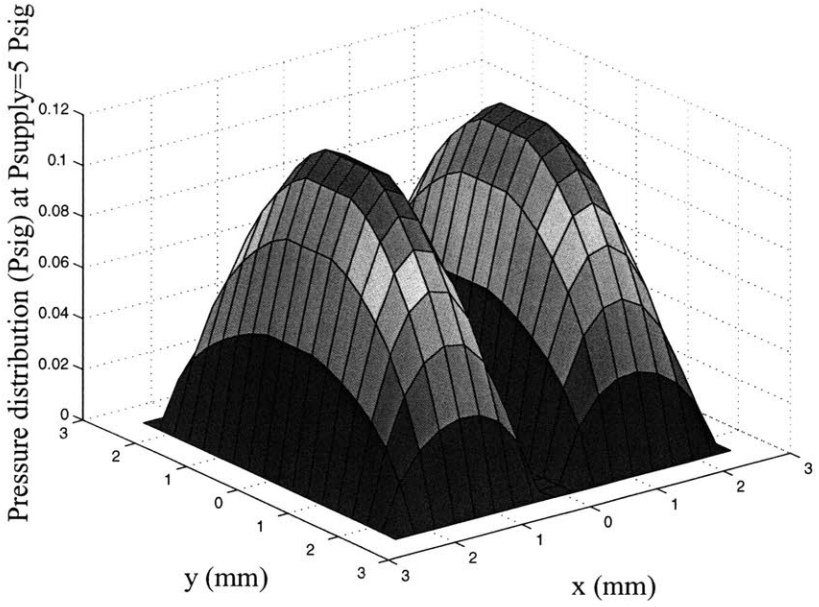

Figure 2-9: The pressure distribution of a 5×5 mm^2 bearing with one central groove 22 μm wide and 50 μm deep.

2.4 Conclusions

Glass is to be slumped on a thin layer of air to obtain the required final glass surface figure. Flow through a porous, rectangular bearing is modeled using Darcy's law. The predicted pressure profile in the air gap between the ceramic and the glass sheet shows a large pressure gradient, almost equal to the supply pressure in magnitude, within the gap. This pressure gradient is diminished with the introduction of grooves onto the surface of the ceramic. The grooves allow for air to leak out to the atmosphere with minimum pressure gradient, $\sim 2\%$ the supply pressure, averaged out throughout the gap, thus obtaining a more uniform pressure distribution.

Chapter 3

Mechanical Properties of Porous Rectangular Bearings

The mechanical behavior of porous ceramic bearings describing their response to mechanical loads is crucial for the proper design of an assembly that functions at elevated temperatures. Material response represents the effects of mechanical loads on defects and atomic motion, which in turn depend on the chemical bonds among the atoms constituting the structure.

Ceramics are formed of metals and non-metals with ionic, covalent, or mixed ionic and covalent bonds, which give them their relatively high compressive strength. The degree of ionic character depends on the electronegativities of the atoms constituting the ceramic. An important drawback of ceramics is their brittle behavior especially under tensile loads because of their inability to accommodate strains in the presence of crack tips.

The material behavior of solids is mostly controlled by the presence of defects in crystal structures. These defects determine how the material responds to factors such as loads, temperature, and the environment. A thorough analysis of individual effects of loads would lead to a better understanding of the combined effects of the different factors that work together to determine the material's true tolerance under given conditions [20].

Loads orthogonal to the x, y, and z axes are tensile if they stretch the solid bound-

aries or compressive if they compress these boundaries. For a small displacement, the system is in the elastic region, where the induced deformation is fully recovered. Elastic deformation can be time dependent, where for a given force, time is required for the atoms to flow through the solid, and once the force is removed, the atoms return to their original positions after a certain period of time has elapsed. The solid is said to be viscoelastic, a state found in polymers, metals, and ceramics. If the force per unit area is sufficiently high, the solid goes through a plastic deformation, where the atoms do not flow back to their original positions after the load is removed. Plastic deformation is permanent and is usually associated with zero volume change.

A moment applied on the solid leads to shear stresses that result in angular displacements. Shear displacements may be elastic, viscoelastic, or plastic; however, the required shear yield stress is much smaller than the required tensile or compressive yield stresses that lead to plastic flow of atoms. It is usually the combination of axial and shear stresses that lead to the plastic flow of materials in most practical engineering problems.

Defects affect the strength of materials, which, with the exception of metals, depends on the primary and secondary bond strengths. The presence of defects leads to the premature failure of the material before the theoretical strength is reached. This is particularly important in brittle materials such as ceramics, where the effects of stress concentrators are severe. Hardness, which is a measure of how tightly the atoms are held together within a material, can be used to understand its strength. Hardness reflects the resistance of a material to penetration by an indenter. Some "rules of thumb" have been developed to estimate the strength of materials from the hardness level. These provide an estimate within 20%, which is adequate for many practical purposes. The yield strength for instance is approximately equal to one-third the hardness level. If the force applied is large enough to lead to the separation of atomic bonds resulting from defects, fracture occurs. Fracture is the result of crack formation and propagation. Ductile materials undergo plastic flow before fracture, where the process of crack formation is relatively slow, whereas brittle materials undergo pure bond rupture, where cracks may spread extremely rapidly, with very

little plastic deformation.

Cyclic loads lead to the formation and growth of cracks at stress levels that are as low as half the theoretical tensile strength. This form of failure is known as fatigue, a catastrophic and insidious failure occuring suddenly. Crack initiation results from pre-existing defects at high stress concentrations such as notches, gas bubble entrapments, or precipitates, with the most intense damage occuring at the surface, where the possibility of having scratches, sharp fillets, threads, and dents is highest. Once these cracks are formed, the remaining life of the material is determined by the number of cycles required to grow the crack to failure at stresses much lower than the yield stress.

The effects of temperature can not be ignored when a solid is placed at elevated temperatures. Thermal fatigue's origin is the restraint to the dimensional expansion and/or contraction that would normally occur in a structure with variations in temperature. Thermal stress σ on a plane strain plate depends on Young's modulus of the material E, the coefficient of thermal expansion α, Poisson's ratio ν, and the temperature change ΔT, and is given by

$$\sigma = \frac{\alpha E}{1-\nu}\Delta T. \tag{3.1}$$

In order to avoid thermal stresses, the restraint source must either be eliminated or reduced to allow for unhindered dimensional changes, or the material must be chosen with appropriate physical properties. Once the thermal stress reaches a critical value, thermal shock occurs depending on the direction of temperature change. A down-shock is the result of quick cooling of the ceramic and causes tensile stresses on the surface of the ceramic and compressive stresses in the bulk. Fracture in this case is sensitive to surface flaws. An up-shock, on the other hand, causes tensile stresses in the bulk and fracture is sensitive to volume flaws. The thermal shock resistance parameter $TSRP$ is used to identify the important material properties regarding fast heat transfer conditions.

$$TSRP = \frac{\sigma_c(1-\nu)k}{\alpha E}, \tag{3.2}$$

Material	Young's modulus GPa	Thermal conductivity W/mK	CTE $10^{-6}/°C$	Knoop hardness HK_{100}	Average pore size μm
SiC	455	155	4.5	27	4
Al_2O_3 (96%)	300	24	7.4	10	0.8
Al_2O_3 (99.7%)	375	28	8.1	14	> 1
Graphite	4.8	24	0.6-4.3		
Al_2O_3:Si	320	1.26	3.6	5	< 1
Si:Nite	310	30	3.3	15	0.5
Al:Nite	330	100	5.0	10	2.5

Table 3.1: Mechanical properties of different engineering ceramics

where σ_c is the critical thermal stress, ν is Poisson's ratio, k is the thermal conductivity, α is the coefficient of thermal expansion, and E is the Young's modulus. Equation 3.2 shows that the TSRP increases as k increases while E and α decrease. This is obvious, since increasing the thermal conductivity of the material decreases the temperature gradient across it, while decreasing the Young's modulus and coefficient of thermal expansion reduce the associated stress for a given strain ($\sigma = E\epsilon$) and strain for a given temperature change($\epsilon = \alpha\Delta T$), respectively. These factors must be kept in mind when selecting a material to be used at varying temperatures.

Another important temperature effect is creep, which becomes more evident as the temperature is raised above the recrystallization temperature (~0.3-0.5 of the absolute melting temperature) of the material. Creep is the time-dependent and permanent deformation of materials when subjected to a constant load, which leads to the flow of defects, the diffusion of grain boundaries, and the formation of microvoids. The smaller the grain size of the ceramic, the higher the likelihood of having creep caused by the larger number of sliding and diffusing grain boundaries.

All these factors influence the behavior of materials and must be taken into consideration for selecting the proper ceramic used to fabricate the porous bearing. Table 3.1 summarizes the mechanical properties of the most prominent pore-free ceramics.

Silicon carbide is the best material to be used in this application because of its high stiffness, high thermal conductivity, low coefficient of thermal expansion and outstanding dimensional stability. However, silicon carbide is extremely hard, and it requires expensive diamond tooling to precision machine it [21].

Nitride ceramics have excellent properties as well but are not commercially available in the porous form. Porous alumina on the other hand is commonly used in various industries, particularly the air bearing industry (New Way Precision and Nelson Air). A rectangular plate with millions of sub-micron holes and a surface flatness of < 1 μm was purchased from Newway Precision. The vendor claims the part to be made of alumina, which typically has a white color; however, the grey color of the part indicates the presence of silicates as well. The properties of 96% alumina are used to predict the stresses and deformations of the part during the thermal process.

3.1 Effect of Porosity on Young's Modulus

Most ceramics are porous. The percentage of porosity varies with different applications. Typical ceramics are 1-20% porous with advanced ceramics having $< 1\%$ porosity. The effect of porosity on the elastic properties of ceramics has been thoroughly investigated, the result being numerous relationships between elastic constants such as Young's modulus, shear modulus or Poisson's ratio and the volume fraction of pores P.

A linear function relates the effective modulus E_{eff} to Young's moduli E_1 and E_2 of a composite material, where the subscript 1 denotes the primary phase and the subscript 2 denotes the secondary introduced phase, which in the case of a porous ceramic is air.

$$E_{eff} = E_1(1 - P) + E_2P. \tag{3.3}$$

E_2 is zero for air. Experiment shows that this model is false for most ceramics especially as the porosity increases. Another attempt uses an exponential function

$$E_{eff} = E_o e^{-bP} \qquad P \leq 0.5 \tag{3.4}$$

$$E_{eff} = E_o e^{-b'P} \qquad P \geq 0.5, \tag{3.5}$$

where E_o is the pore-free Young's modulus, and b and b' are empirical parameters without a clear relationship to the porosity of the microstructure. Equation 3.4 seems to agree for $P < 0.2$, whereas Equation 3.5 is not valid for most ceramics.

A power function relating between Young's modulus and porosity is

$$E_{eff} = E_o(1 - aP)^n, \tag{3.6}$$

where a is the pore connectivity factor describing the array assembly of pores, such that pores are not interconnected when $a = 1$, and n is the pore shape factor. The pores are spherical for $n < 2$, and they are irregular in shape for $3 < n < 4$. Porosity can be related to a by

$$a = \frac{1}{P_c}, \tag{3.7}$$

where P_c is the critical porosity, such that when $P = P_c < 1$, $E = 0$, that is the stiffness is completely lost. This means that when $a \rightarrow 1$, $P_c \rightarrow 100\%$, which contradicts the definition of a at $P_c < 1$. This also means that pores are not connected ($a = 1$), yet the stiffness is completely lost, which is physically impossible.

Several other models have been formed to describe the relationship between porosity and Young's modulus; however, almost all these models disregard some of the important factors such as pore size, shape, orientation, distribution, volume fraction, degree of separation, homogeneity, and degree of contiguity, which describes the degree of particle contact of one phase in a two-phase structure.

Fan and co-workers [22] used both geometrical and topological parameters to come up with a model for a two-phase structure composed of α and β particles with total volume fractions of f_α and $f_\beta = 1 - f_\alpha$, respectively, and any grain size, grain shape and phase distribution, as shown in Figure 3-1.

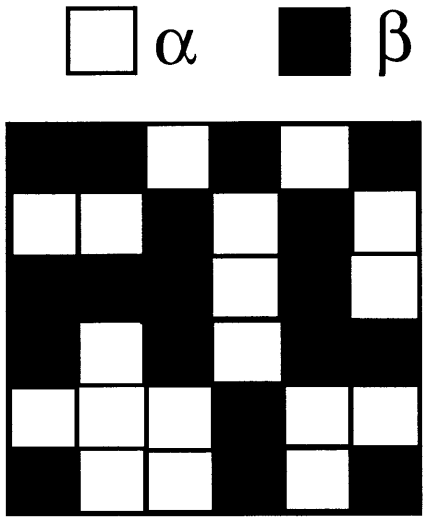

Figure 3-1: A schematic representation of a microstructure composed of randomly distributed α and β phase particles

Figure 3-2 shows the topological transformation of the microstructure in Figure 3-1. These microstructures are mechanically equivalent along the aligned direction of the microstructure in Figure 3-2 [23]. This new structure consists of a continuous α-phase with a volume fraction of $f_{\alpha c}$, a continuous β-phase with a volume fraction of $f_{\beta c}$, and a long-range of $\alpha - \beta$ chains with a volume fraction F_s. These are regions EI, EII, and EIII, respectively, where the last region contains only phase boundaries.

The volume fractions of the α- and β- phases ($f_{\alpha III}$ and $f_{\beta III}$, respectively) in region EIII can be calculated by

$$f_{\alpha III} = \frac{f_\alpha - f_{\alpha c}}{F_s} \tag{3.8}$$

$$f_{\beta III} = 1 - f_{\alpha III}. \tag{3.9}$$

The microstructure in Figure 3-2 is easier to analyze, yet since it is equivalent to the original microstructure, the relationship between Young's modulus and porosity can be determined. Fan used statistics and probability to derive the topological parameters, which must usually be measured experimentally; however, if random

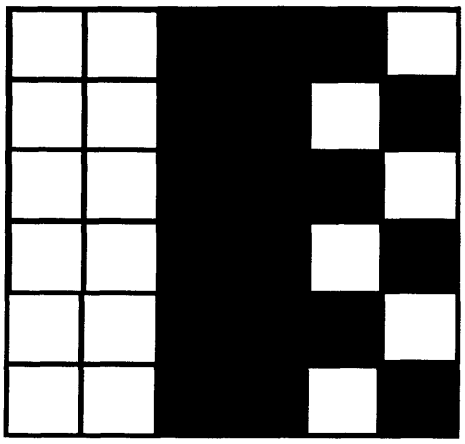

Figure 3-2: Topological transformation of microsturcture shown before to an equivalent model

distribution of equiaxed particles is assumed, the following relationships hold.

$$f_{\alpha c} = \frac{f_\alpha^2 d_\beta}{f_\beta d_\alpha + f_\alpha d_\beta} = \frac{f_\alpha^2 R}{f_\beta + f_\alpha R} \tag{3.10}$$

$$f_{\beta c} = \frac{f_\beta^2 d_\alpha}{f_\beta d_\alpha + f_\alpha d_\beta} = \frac{f_\beta^2 R}{f_\beta + f_\alpha R} \tag{3.11}$$

$$F_s = 1 - f_{\alpha c} - f_{\beta c}, \tag{3.12}$$

where d_α and d_β are the grain sizes of the α- and β-phases, respectively, and R is the ratio of these grain sizes such that $R = \frac{d_\beta}{d_\alpha}$. Boccaccini and Fan show that $R = 1$ overestimates the Young's modulus at low porosity ($P \leq 0.25$). However, for intermediate porosity levels ($0.25 \leq P \leq 0.5$), $R = 1$ better predicts experimental data than when lower values of R are used. For lower values of porosity, $0.4 \leq R \leq 0.6$ shows a better correlation with experimental results. For accuracy, R should be determined using metallographic measurements, since there is no clear relationship between R and porosity.

The porosity of the material can be calculated if its density is known. The density of the pore-free ceramic ρ_o can be found in literature. The density of the porous ceramic ρ is measured using the Archimedes method. Porosity is defined as

$$P = f_\beta = 1 - \frac{\rho}{\rho_o}, \tag{3.13}$$

where f_β is the volume fraction of the β-phase.

Fan and co-workers derived the equation for the effective Young's modulus E_{eff} to be

$$E_{eff} = E_\alpha f_{\alpha c} + E_\beta f_{\beta c} + \frac{E_\alpha E_\beta F_s}{E_\beta f_{\alpha III} + E_\alpha f_{\beta III}}, \tag{3.14}$$

where E_α and E_β are the Young's moduli of the pure $\alpha-$ and $\beta-$phases, respectively. In the case of a porous ceramic, $E_\beta = 0$ and Equation 3.14 reduces to

$$E_{eff} = E_\alpha f_{\alpha c}. \tag{3.15}$$

The Young's modulus and density of pore-free alumina are 300 GPa and 3.7 g/cm^3, respectively. The density of the porous material is calculated to be 2.68 g/cm^3. Therefore, using Equation 3.13, the porosity of the plate or f_β is $\sim 30\%$, and $f_\alpha = 1 - f_\beta$ is 70%. Using these values of the volume fraction of the α- and β-phases in Equation 3.10 with $R = 1$, the volume fraction of the continuous α-phase is calculated to be 0.49. The effective Young's modulus is thus found from Equation 3.15 to be 147 GPa. Figure 3-3 shows the dependence of the Young's modulus of Al_2O_3 (96%) on porosity.

3.2 Effect of Temperature on Young's Modulus

The effect of creep at elevated temperatures on the shear modulus G_o of alumina ceramics was reported by Ashby and Frost [24]. For alumina, this effect is prominent at temperatures higher than $0.5T_M$, where T_M is the melting temperature of alumina. Ashby and Frost tabulate the coefficients of temperature dependence of modulus

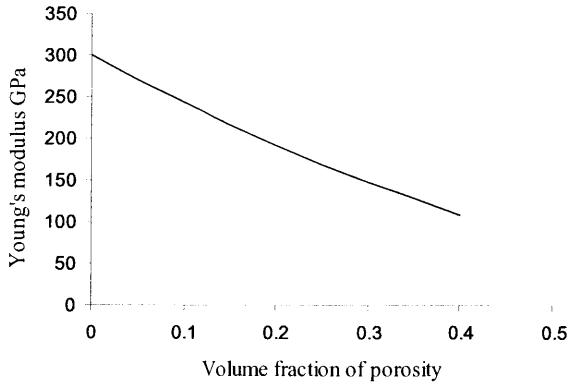

Figure 3-3: The dependence of Young's modulus on the porosity of an alumina ceramic

$\frac{T_M}{G_o}\frac{dG}{dT}$ for various materials with a value of -0.35 for alumina. The relation between the shear modulus G_o at 300K and G at the elevated temperature is

$$G = G_o\left(1 + \frac{T - 300}{T_M}\left(\frac{T_M dG}{G_o dT}\right)\right). \tag{3.16}$$

For isotropic materials, the shear modulus G is related to Young's modulus E by

$$G = \frac{E}{2(1+\nu)}, \tag{3.17}$$

where ν is the Poisson's ratio and equals 0.22 for alumina. Using Equation 3.17 with the proper value of E to account for porosity, the shear modulus G_o at 300K is 60.25 GPa. The melting temperature of alumina is 2320K; therefore, using Equation 3.16, the shear modulus at 650°C or 923K is 54.59 GPa. Using Equation 3.17 one more time, the effective Young's modulus for a porous alumina plate at 650°C is 133.2 GPa.

3.3 Machining Grooves on the Ceramic Surface

Several methods have been considered for machining grooves on the surface of the porous ceramic [25]. Electron beam machining (EBM) uses a high velocity stream of electrons focused on the workpiece to remove material by melting and vaporization with a beam diameter as small as 0.025 mm. The advantages of EBM include the

tight tolerances on very thin slots with no cutting forces or tool wear; however, the operation must be performed in vacuum to eliminate collision of electrons with gas molecules, and high energy is required for the process, not to mention the expensive equipment, and the duration of the process for machining deep and long grooves. Laser beam machining (LBM) uses the light energy from a laser to remove material by vaporization and ablation. This process is extremely slow and expensive. Ultrasonic machining, where abrasives contained in a slurry are driven at high velocity against the work by a tool vibrating at low amplitude but high frequency perpendicular to the work surface, is excellent for drilling holes but not slots.

The grooves on the porous ceramic have been diamond sawed. This process is not as accurate as the non-traditional methods described above; however, the cost effectiveness and high material removal rate are tempting at this stage of the experiment. The size of the grooves is limited by the feasibility of using a thin saw blade without suffering from the effect of the blade wobbling that would cause variations in dimensions along one groove, and from groove to groove. The width of the grooves is 305 μm with a depth of 1 mm. The spacing between two consecutive grooves is 457 μm. The optic surface area is 140×100 mm^2. The bearing area must be slightly smaller than the optic area to avoid air leakage from the edges, where a low resistance to flow dominates. A total of 182 grooves over a length of 139.38 mm are machined. Figure 3-4 shows the top view of the grooves machined on a pore-free alumina ceramic as seen under an optical microscope. The width variation is < 10 μm except at the very edge, where the saw is introduced into the part.

After machining grooves on the top surface of the ceramic, the valleys and side walls of the grooves must be sealed to avoid air from leaking through the grooves but rather go out of the peak regions to lift the glass. The best method for coating such narrow yet deep grooves is the chemical vapor deposition (CVD) process. A vapor phase known as the precursor, diluted with a carrier gas, reacts at a hot surface, where a solid thin film is deposited. After the diffusion of the precursor molecules to the hot surface, they get adsorbed to the surface, decompose, and the molecular byproducts recombine and desorp into a gas phase that is carried away from the

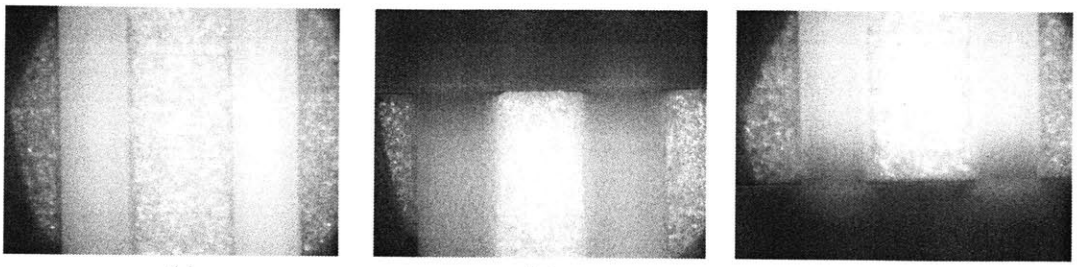

(a) *(b)* *(c)*

Figure 3-4: Top view of grooves (0.305 mm wide and 1 mm deep) machined on a pore-free alumina part. *(a)* shows the central region of the bearing, *(b)* shows the end, where the saw was introduced to the part, and *(c)* shows the other end.

deposition zone [26].

To avoid problems associated with a difference in the coefficient of thermal expansion (CTE) between the substrate and the thin film during the process of heating the ceramic to the slumping temperature, it is necessary to use a coating with a similar CTE as alumina, which itself is a material commonly used in CVD coatings. A customized alumina coating for a part with deep trenches has been found to be costly; therefore, a commercial coating by Richter Precision has been selected for this application. The coating known as the *Titankote H5* is composed of 1 μm of TiN, 2-3 μm of TiCN/TiC, and 3-4 μm of alumina [27]. Figure 3-5 shows the cross-section of coated grooves of a pore-free alumina part, as seen by an optical microscope.

Porous alumina is more susceptible to fracture upon machining due to its decreased stiffness. This is clear in Figure 3-6 showing the grooves sawed following the same procedure as for the pore-free alumina parts. The integrity of the coating can not be evaluated using the optical microscope due to the large thickness of the part, and the lack of space to place it under the microscope.

3.4 Housing Design

The two design criteria for the housing are related to the material selected and the method of constraining the porous part with minimum stresses and deformations.

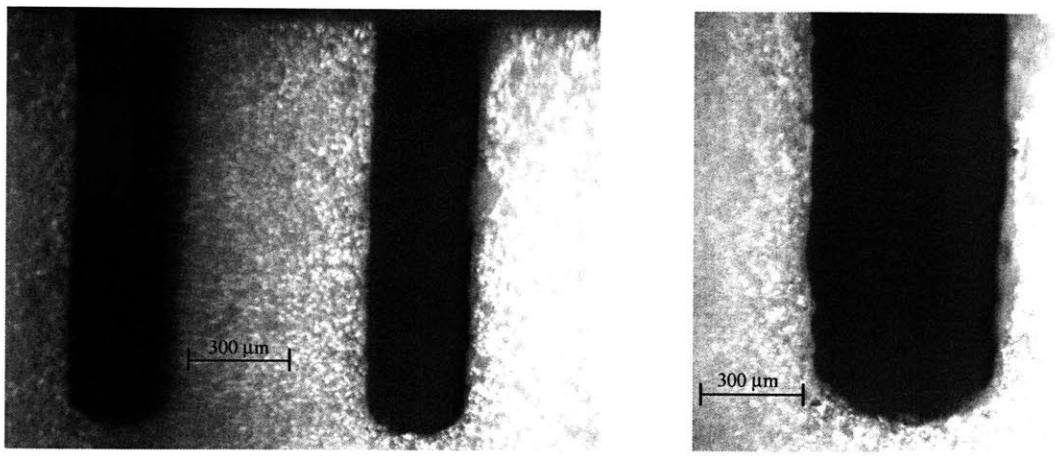

Figure 3-5: Cross-sectional view of a pore-free alumina coated with *Titankote H5* by Richter Precision using CVD. *(a)* shows two coated grooves, whereas *(b)* shows a magnified view of one of the grooves.

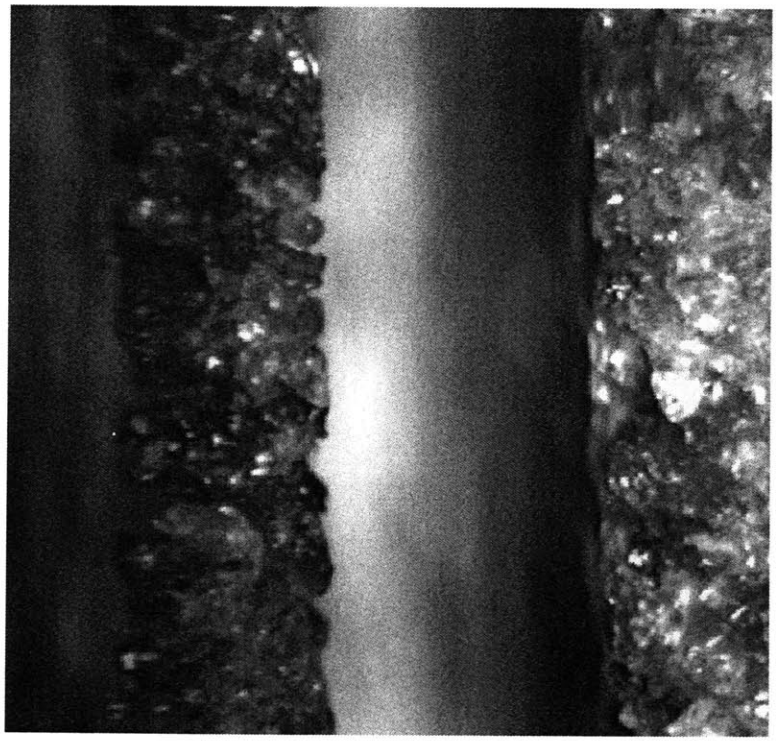

Figure 3-6: Top view of grooves machined on a porous alumina ceramic. The quality and tolerance on groove geometry is inferior when compared to those on the pore-free part.

Material	Young's modulus	Thermal conductivity	CTE	Creep	Machinability	Cost	Total
Cu	+	+	-	-	-	0	-
Re	-	0	+	+	-	-	-
Mo	-	+	+	+	-	-	0
W	-	+	+	+	-	-	0
SiC	0	+	+	+	-	-	+
SS	+	-	-	0	-	0	-
Al_2O_3	0	-	+	+	-	+	+

Table 3.2: Properties of different materials considered for manufacturing the air bearing housing.

3.4.1 Material Selection

When selecting the material for the housing, where the air plenum for the porous ceramic is found, several factors must be taken into consideration. The porous ceramic is brittle. Thermal stresses induced by the housing constraining this ceramic must be minimized to avoid its failure. The housing material must withstand the high temperatures with minimal creep; therefore, as its melting temperature increases, its Young's modulus and hardness will increase as well, making its machining a tedious task. It is preferable to use a material with a rather high conductivity to decrease temperature gradients in the air before it goes through the porous medium. Table 3.2 summarizes the advantages and disadvantages of several materials taken into consideration for this assembly.

Silicon Carbide is the best candidate for this application; however, for the same reasons mentioned before, it has been decided not to use it at this stage. By using the same material as the porous ceramic for the housing, thermal mismatch stresses would be eliminated. Alumina is very hard to machine when it is fully fired to its final brittle state; therefore, the basic geometry of the housing must be accomplished in the green state of alumina, that is before it is fired and hardened, using standard CNC machining. The tolerance on the dimensions is very poor in this case given the

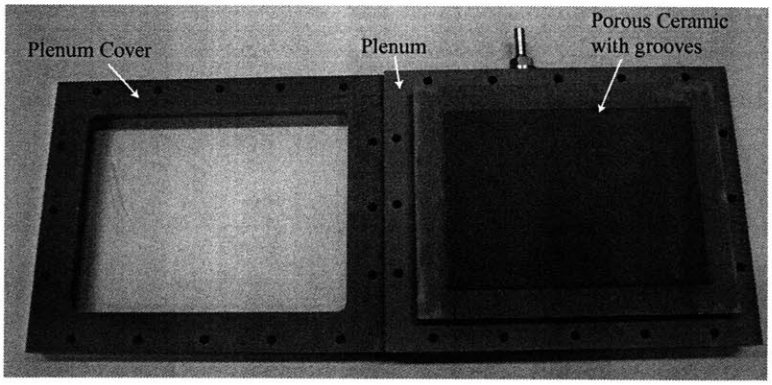

Figure 3-7: Housing to constrain the porous ceramic and provide a sealed pressure plenum.

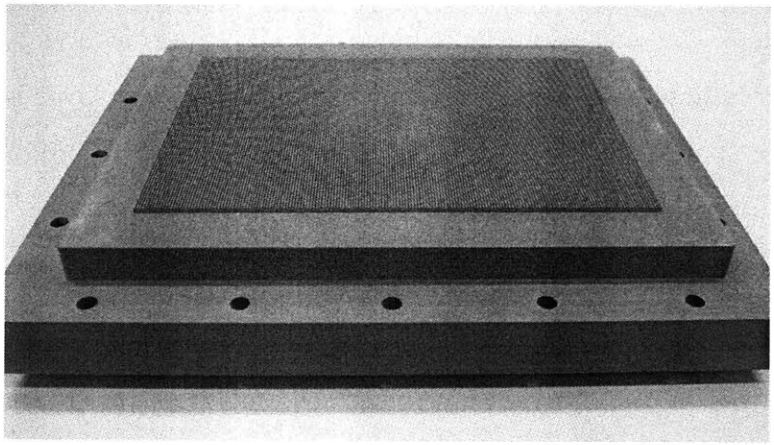

Figure 3-8: Grooves machined on porous alumina ceramic.

fact that alumina shrinks by approximately 20% after it is fired.

Machinable alumina silicate, which is not fully fired, is commercially available. It has a porosity of 1-2% and can be machined using carbide tools. This material has been selected for the housing because it is similar to the porous ceramic material. Two parts constitute the housing, as shown in Figure 3-7, the plenum on which the porous ceramic rests and the cover, which seals the plenum and fully constrains the porous medium. Figure 3-8 shows the porous part with the grooves on the top surface.

3.4.2 Joint Design

The interface between the two alumina silicate parts must be properly sealed to avoid low resistance pathways, where air would leak out of the plenum rather than go through the porous medium. The two methods considered are brazing and bolted joints. The interface must withstand the high slumping temperature.

Brazing

A common braze layer is composed of an alloy of copper, gold, and traces of titanium [28] with an average CTE of $16 \times 10^{-6}/°C$, and a layer thickness ranging between 12.5 and 25 μm. The difference between the CTE of the braze layer and the alumina part leads to thermal stresses as the assembly temperature is raised and lowered by 650°C. To estimate the stresses in the braze layer, a layer of thickness t_b is sandwiched between two ceramic parts of thicknesses t_{c1} and t_{c2}. The braze layer is much thinner than the ceramic parts; the stress in this layer is assumed to be uniform throughout the thickness. At equilibrium

$$\sigma_b t_b = \sigma_c (t_{c1} + t_{c2}), \tag{3.18}$$

where σ is the stress in the different layers with the subscripts b, $c1$, and $c2$ representing the braze layer, ceramic part one and ceramic part two, respectively. The stresses and strains in the plane parallel to the interface between the different parts are the same in all directions within that plane; therefore, Hooke's law reduces to

$$\sigma = \epsilon \frac{E}{1-\nu}, \tag{3.19}$$

where ϵ is the thermal strain, E is Young's modulus, and ν is Poisson's ratio. Substituting Equation 3.19 into Equation 3.18 the following relation holds

$$\epsilon_b \frac{E_b}{1-\nu_b} t_b = \epsilon_c \frac{E_c}{1-\nu_c} (t_{c1} + t_{c2}). \tag{3.20}$$

As the temperature of the assembly is increased, the final length of both brazing layer and ceramic parts is L_f. Thermal strain is represented by

$$\epsilon_b = \frac{(L_f - L_b)}{L_b} \tag{3.21}$$

$$\epsilon_c = \frac{(L_f - L_c)}{L_c}, \tag{3.22}$$

where L_b and L_c represent the lengths the braze layer and the ceramic would have gone if they had been seperate at the elevated temperature, respectively. L_b and L_c are represented by

$$L_b = L_i(1 + \alpha_b \Delta T) \tag{3.23}$$

$$L_c = L_i(1 + \alpha_c \Delta T), \tag{3.24}$$

L_i being the initial length of all layers. By combining Equations 3.20 through 3.24, the strain in the braze layer can be expressed by

$$\epsilon_b = \frac{A(\alpha_b - \alpha_c)\Delta T}{1 + \alpha_c \Delta T + A(1 + \alpha_b \Delta T)} \tag{3.25}$$

$$A = \frac{t_{c1} + t_{c2} E_c (1 - \nu_b)}{t_b E_b (1 - \nu_c)}. \tag{3.26}$$

For $t_{c1} = t_{c2} = 25.4$ mm, $\alpha_b = 16 \times 10^{-6}/°\text{C}$, $\alpha_c = 8.5 \times 10^{-6}/°\text{C}$, $E_c = 360$ GPa, $E_b = 90$ GPa, $\nu_c = 0.22$, $\nu_b = 0.37$ and $\Delta T = 600°\text{C}$, the strain in the braze layer is 4.5×10^{-3}. Using Equation 3.19, the corresponding thermal stress is 643 MPa, which is higher than the tensile strength of the braze layer resulting in joint failure. Therefore, a bolted joint is considered instead.

Bolted Joint

The second alternative to assemble the two parts is by using bolts. In order to eliminate the use of a gasket that must withstand high temperatures, the mating surfaces of the ceramic parts are lapped flat, and the bolts are placed such that the

cone of influence of every bolt overlaps with the cone of the adjacent bolt. This insures that the two surfaces fully seal the plenum.

Titanium bolts with a CTE very close to that of alumina are used to join the two parts to avoid joint loosening caused by bolt over-expansion, which is further compensated by the addition of spring washers.

The porous ceramic must be fully constrained to eliminate vibration that could cause the fracture of the ceramic due to fatigue. To estimate the deformation δ of the porous part due to the pressure in the plenum, it is modeled as a fully constrained beam with a distributed load F equal to the pressure in the plenum multiplied by the area of the porous ceramic.

$$\delta = \frac{FL^3}{384EI}, \tag{3.27}$$

where L is the length of the bearing, E is Young's modulus for the porous bearing at elevated temperatures, and I is the moment of inertia. Experiment shows that a pressure as low as 1 Psig is enough to lift a thin rectangular optic using the grooved bearing before applying the CVD coating. Therefore, for this pressure, the deflection of the ceramic is 2.17 μm. This deformation will be replicated on the surface of the optic; therefore, in the future, an additional grinding process may be needed to start with a concave surface and end up with a flat one once the pressure is turned on.

3.5 Conclusions and Future Work

The effects of porosity and temperature on the mechanical integrity of the alumina ceramic have been investigated. A porosity of 30% reduces the stiffness of the ceramic by $\sim$ 50%, whereas increasing the temperature by 630°C further reduces it by $\sim$ 9%. This decrease in stiffness is evident in the inferior quality of the grooves machined on the surface of a porous part as compared to those on a pore-free ceramic.

In order to properly perform the slumping procedure using a porous, grooved ceramic, the supplied air carrying the optic must be at the slumping temperature before it touches the surface of the foil to reduce temperature gradients and associated

viscosity variation in the optic bulk. This requires a couple of meters of supply tube twisted in the furnace at 650°C before it is connected to the assembly. The current furnace volume is too small for this to be possible. A new furnace that can accomodate the assembly and the tubes has been purchased but not received yet. The future work will involve slumping a thin rectangular sheet on a CVD-coated ceramic with the goal of changing the surface flatness from hundreds to a couple of microns.

Chapter 4

Thin Optic Metrology Truss

Over the past few years, progress has been made in the shaping and accurate assembly of the thin foils used in x-ray reflecting mirror modules. The enabling technology for further improvements lies in the advances of surface metrology of thin optics. The design of a kinematic optic holder that can be used to accurately measure the free-form surface topography of thin optics and thus evaluate their shaping processes is required. This device minimizes the effects of external loads acting on the optic such as gravity induced sag, frictional forces during optic manipulation, and thermal stresses. The significant effects of these loads contribute to the deformation of thin optics, leading to inaccurate surface maps [29]. The optics of interest include borosilicate glass and single-crystal silicon with rectangular (100 mm×140 mm×0.4 mm) and circular (diameter 100 mm×0.4 mm) geometries, as shown in Figure 4-1.

The device will be used in conjunction with a Shack-Hartmann surface metrology system to provide accurate and repeatable surface maps [8]. The maximum tolerable deformation due to the optic's surface non-flatness, the external forces mentioned above, and the repeatability of the metrology tool is 500 nm. A pitch repeatability of 70 arcsec is required to limit gravity sag deformation to 50 nm. These high-level functional requirements have been defined based on the resolution of the metrology tool, the expected warp of the optic after the shaping process, and gravitational sag and friction force modeling previously completed [31].

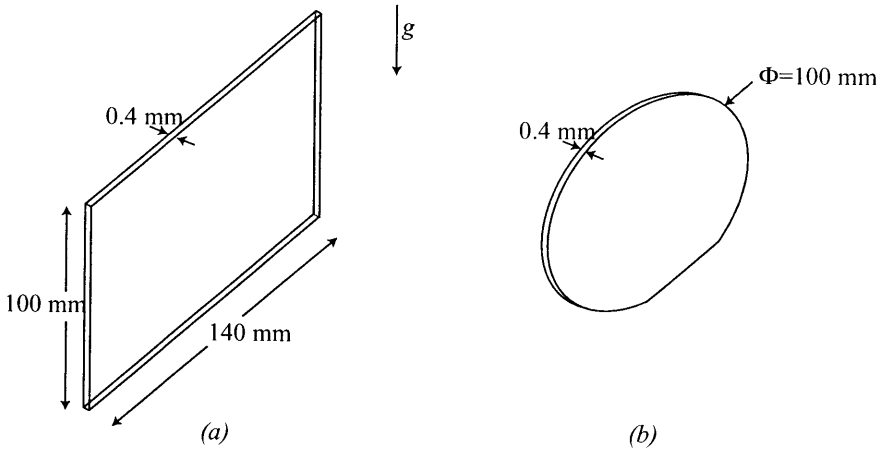

Figure 4-1: The dimensions of (a) rectangular and (b) circular glass and silicon optics.

4.1 Strategies

Different ways of optic constraint have been considered to account for the major external forces that deform thin foils. These strategies are divided into two groups: horizontal and vertical mounting schemes, where the latter is further divided into subgroups.

4.1.1 Horizontal Placement

This method utilizes three pins placed $0.577L$ apart, L being the length of the optic along the direction of every pair of pins, to minimize gravity sag [32]. Knowing material properties, the effect of gravity can be removed using finite element analysis (FEA). The major concern is associated with the optics' unknown thickness variation; D 263 borosilicate rectangular glass sheets manufactured by Schott have a thickness variation of ± 20 μm. To account for the error associated with such variations, the optic is modeled as a simply-supported beam with a uniform load as shown in Figure 4-2.

The maximum deformation δ_{max} at the optic's centerline is given by

$$\delta_{max} = \frac{5F(0.577L)^3}{384EI}, \tag{4.1}$$

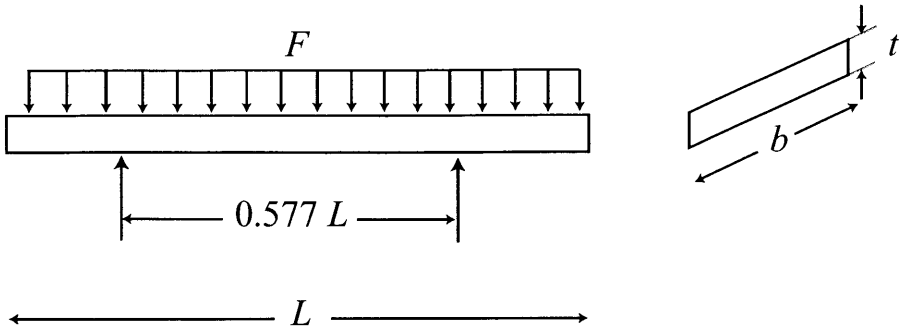

Figure 4-2: Horizontal placement of an optic modeled as a simply-supported beam with the optic weight acting as a uniformly distributed load.

where F is the weight per unit length, L is the length of the optic, E is Young's modulus, and I is the moment of inertia. The weight per unit length is

$$F = \frac{\rho b t L g}{L}, \tag{4.2}$$

where ρ is the density of the optic, b is the width, t is the thickness, and g is the gravitational acceleration. The moment of inertia is

$$I = \frac{bt^3}{12}. \tag{4.3}$$

Substituting Equations 4.2 and 4.3 into Equation 4.1, the maximum deformation is given by

$$\delta_{max} = \frac{\rho g L^4}{57.74 E t^2}. \tag{4.4}$$

Table 4.1 summarizes the properties of the D 263 glass and silicon optics. Figure 4-3 shows plots of optic deformation when placed horizontally versus different thickness values, and change in deformation versus thickness variation for D 263 glass optics. Figure 4-3(b) shows that the error associated with the optic's thickness variation ranges between -0.75 μm to 0.87 μm, which are beyond the tolerance of 0.5 μm. FEA sag removal accuracy depends on the optic's thickness variation, placement repeatability, and material homogeneity.

	ρ	E	ν	Dimensions	α
	g/cm^3	GPa		mm	$10^{-6}/°C$
D 263	2.53	72.9	0.208	$140 \times 100 \times 0.4$	~ 7
				$\phi 100 \times 0.4$	
Silicon	2.33	130	0.18	$\phi 100 \times 0.4$	2.3

Table 4.1: Properties of D 263 glass and silicon wafers

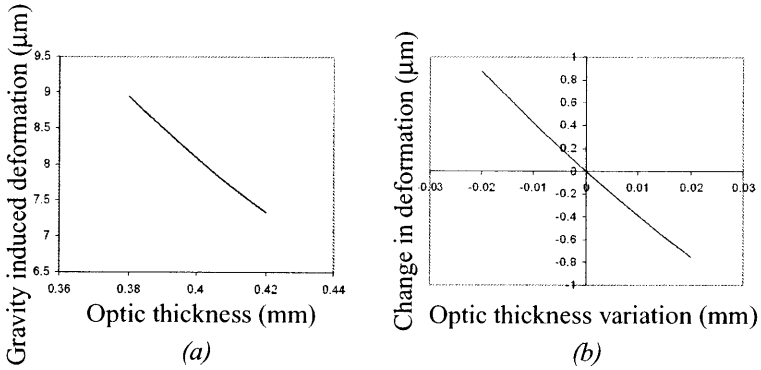

Figure 4-3: The dependence of optic deformation on the thickness variation of the optic. (a) shows deformation of optics with different thicknesses, and (b) shows the change of deformation when the optic thickness is different from the reported 0.4 mm.

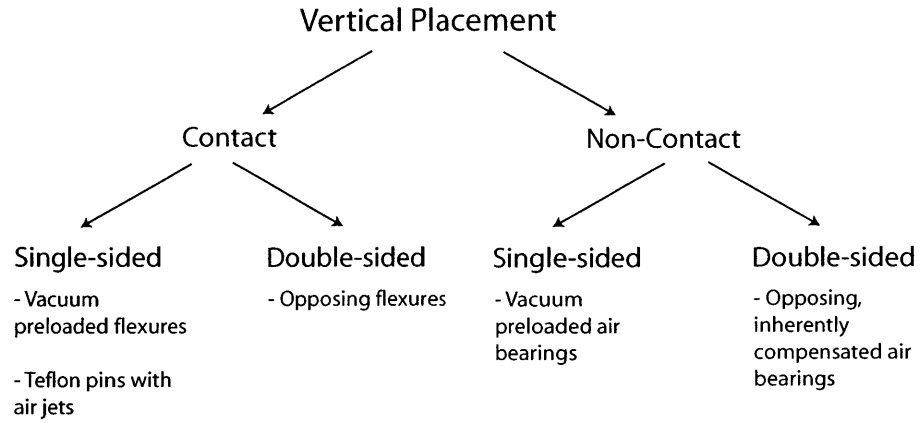

Figure 4-4: Different vertical placement strategies for constraining thin optics.

4.1.2 Vertical Placement

Upon holding the optic in the vertical plane, the effects of gravity are eliminated. Several strategies are developed for vertical placement as shown in Figure 4-4.

Vacuum Preloaded Flexures

Three, hollow, long tubes acting as flexures constrain the optic using vacuum through the tubes. The points of contact are shown in Figure 4-5. Since friction between the tube and the optic is the only carrying force, the inner diameter of the tube is dimensioned such that the force resulting from a practical vacuum of 413.76 mm of Hg (8 psi) can carry the weight of the optic.

The tubes considered for this strategy are stainless steel precision tubes for their availability and low cost. The load on the flexures is the weight of the rectangular glass sheet, which is equal to 0.139 N with a factor of safety of 5 to allow for the constraint of thicker optics as well. This load is equally distributed among the three flexures. The friction force f is

$$f = \mu V A, \tag{4.5}$$

where μ is the coefficient of friction, V is vacuum, and A is the area of the hollow section given by

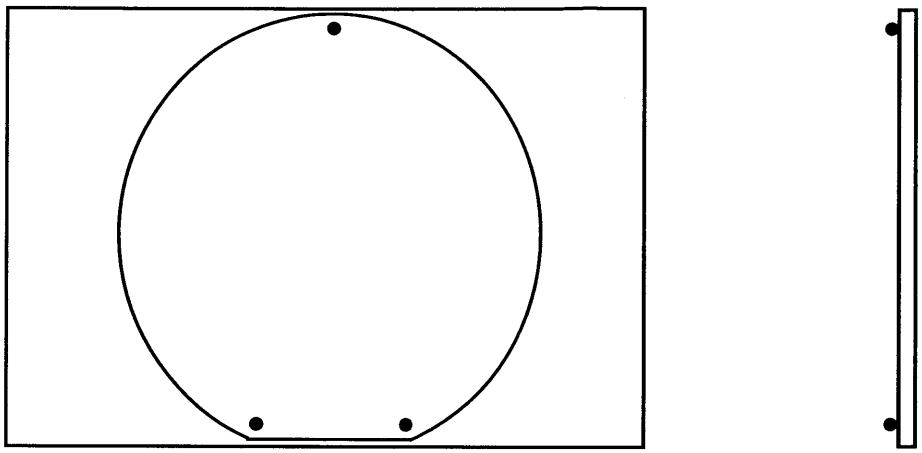

Figure 4-5: Front and side views of overlaying circular and rectangular optics with constraint points represented by small dark circles

$$A = \frac{\pi d_i^2}{4}, \tag{4.6}$$

where d_i is the inner diameter of the tube. Combining Equations 4.5 and 4.6, the required inner diameter is

$$d_i = \sqrt{\frac{4f}{\pi \mu V}}. \tag{4.7}$$

Therefore, for $f = 0.23$ N/flexure, $\mu = 0.5$ between glass and metal [33], and $V = 413.76$ mm of Hg, the resultant inner diameter is 3.26 mm. This places a lower limit on the outer diameter d of the tube, which has to be as small as possible to minimize contact with the optic.

The most critical flexure is the one at the top of the glass when it comes to thermal expansion mismatch compensation. The room temperature where this device is to be placed changes at an average of 1°C per reading. The material for the foil optic holder is chosen to be aluminum for its low cost, availability and ease of machining. The first-order model for thermal expansion is

$$\Delta L = L \alpha \Delta T, \tag{4.8}$$

where ΔL is the change in length, α is the coefficient of thermal expansion, and ΔT is the temperature change. The coefficient of thermal expansion for aluminum and silicon are $23 \times 10^{-6}/°\text{C}$ and $2.3 \times 10^{-6}/°\text{C}$, respectively. Silicon is used for the design parameters because some glass optics, such as Hoya SD-2, have a coefficient of thermal expansion very similar to that of silicon, which is lower than borosilicate glass. Therefore, the differential change in length between the aluminum and the silicon optic over 100 mm of length and 1°C temperature change is calculated to be 2.07 μm. This value corresponds to the displacement δ of the flexure tip. For a cantilevered beam, lateral and angular deflections are

$$\delta = \frac{3EI}{L^3} \tag{4.9}$$

$$\theta = \frac{2EI}{L^3}. \tag{4.10}$$

Combining Equations 4.9 and 4.25

$$\frac{\theta}{\delta} = \frac{1.5}{L}. \tag{4.11}$$

During metrology, the optic is placed in front of a reference flat used to align the device with the vertical plane. Therefore, to minimize flexure straightness errors and the distance between the optic and the reference flat, it is desired to keep the length of the flexures below 50 mm. From Figure 4-6, the displacement x of the flexure tip from the vertical plane is found to be

$$x = d \sin\theta. \tag{4.12}$$

For $L = 50$ mm, $d = 3.5$ mm ($d_i = 3.26$ mm), and $\delta = 2.07$ μm, which corresponds to $\theta = 62.1$ μrad from Equation 4.11, x is found to be 0.217 μm. Since the optic is forced against the flexure tip by vacuum, it will have a local deformation of 0.217 μm as well. This is a local deformation that will be magnified at the free ends of the optic 70 mm away from the flexure tip, therefore exceeding the tolerance of 0.5 μm surface flatness.

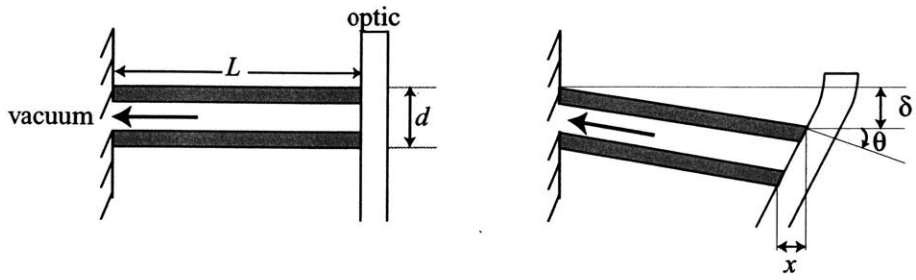

Figure 4-6: The deviation of the tip of the flexure from the vertical plane caused by an increase in temperature during metrology, and the resulting effect on the optic attached to the tip.

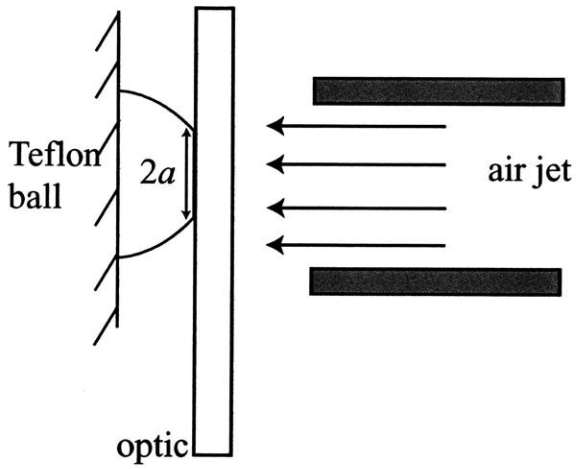

Figure 4-7: A thin optic pushed against a Teflon ball by means of an air jet.

Teflon Pins with Air Jet Preload

This strategy utilizes three low-friction Teflon pins on a reference plane. The optic is held against these pins using air from nozzles on the other side as shown in Figure 4-7.

The most important parameter in this strategy is the preload force from the air jet. In order to reduce the effects of compressibility of air (cooling as it exits the nozzle), the Mach number M defined as the ratio of velocity of air against the speed of sound must be kept less than 0.3 [34]. The speed of sound c at room temperature is 340 m/s; therefore, the maximum velocity of the air from the nozzle is Mc, which is equal to 100 m/s. The preload force F from the air jet is [35]

	E	ν	R_{major}	R_{minor}	α
	GPa		mm	mm	$10^{-6}/°C$
D 263	72.9	0.208	∞	∞	~ 7
Teflon	3	0.4	50	50	100

Table 4.2: Properties of D 263 glass wafers and Teflon balls

$$F = \rho A V^2, \tag{4.13}$$

where ρ is the density of air, A is the inner area of the nozzle, and V is the velocity of the air stream. Since the air stream does not provide for any stiffness, the preload force is chosen to be greater than 0.1 N to make sure that the optic remains stable against the Teflon pins during metrology. The density of air at room temperature and pressure is 1.22 Kg/m^3; therefore, from Equation 4.13 and using the maximum allowable velocity for smallest nozzle area, the corresponding diameter is 3.23 mm.

To calculate the Hertzian contact patch diameter, the model of a sphere against a plane is used. The equivalent Young's modulus E_{eq} is [11]

$$E_{eq} = \frac{1}{\frac{1-\nu_1^2}{E_1} + \frac{1-\nu_2^2}{E_2}}, \tag{4.14}$$

where ν_1, E_1, and ν_2, E_2 are the Poisson's ratio and Young's modulii of Teflon and glass, respectively. Table 4.2 summarizes the properties of D 263 glass and Teflon.

Using these values, the equivalent Young's modulus is found to be 3.94 GPa. The equivalent radius R_{eq} using a 50 mm diameter Teflon ball is [11]

$$R_{eq} = \frac{1}{\frac{1}{R_{major}} + \frac{1}{R_{minor}}}. \tag{4.15}$$

For a sphere, R_{major} and R_{minor} are equal to the radius of the ball; therefore, the equivalent radius is 25 mm. The Hertzian patch radius a is

$$a = \left(\frac{3FR_{eq}}{2E_{eq}}\right)^{\frac{1}{3}} = 98.9\ \mu\text{m}. \tag{4.16}$$

Since the patch diameter is smaller than the air stream diameter, local torques are found on the optic. FEA is used to evaluate the effect of the local torques on the optic surface. The resulting deformation is 0.262 μm, close to half the maximum tolerance of 0.5 μm. This leaves little room for errors from other sources such as gravity alignment, Teflon and nozzle centerline misalignment, and system placement repeatability. As the stream of air leaves the nozzle at high speeds and expands, it cools causing temperature gradients on the optic. This is discussed in detail in Section 1.2.1.

Double-Sided Flexures

This strategy utilizes three pairs of flexures on each side of the optic located at the same positions, as was shown in Figure 4-5. These flexures can accommodate friction and thermal expansion mismatch between optic and device. Several designs have been considered with different sizes. The preliminary design uses 12 mm long tubes with 0.62 mm diameter. The axial stiffness k_{axial} is

$$k_{axial} = \frac{EA}{L}. \tag{4.17}$$

The lateral stiffness is

$$k_{lateral} = \frac{3EI}{L^3}. \tag{4.18}$$

For the dimensions given above, the axial stiffness is 1.78 $N/\mu m$ and the lateral stiffness is 0.00089 $N/\mu m$ giving a ratio of lateral to axial stiffness of 0.0005. To calculate the forces that would cause this flexure to buckle, Euler's buckling theorem is used [36], where the critical force $P_{critical}$ is

$$P_{critical} = A\frac{\pi^2 E}{\left(\frac{L_e}{\rho}\right)^2}, \tag{4.19}$$

where L_e is the equivalent length of the column. $L_e = 2.1L$ for a cantilevered beam, ρ is the radius of gyration defined as the square root of the quotient of the moment of inertia and the cross-sectional area, E is Young's modulus, and A is the cross-sectional

area. For the aluminum flexure with the preliminary design dimensions, the critical load is 20 N. Once this load is exceeded, the slightest lateral displacement causes an eccentric bending moment greater than the internal elastic restoring moment, and the flexure collapses. Such a large force of 20 N is not anticipated upon using the device during metrology.

The major concern is the misalignment of the centerlines of the two opposing flexures. This error is reduced by utilizing monolithic flexures rather than individual opposing ones. This strategy is taken into the concept development level, where the geometry of the flexures is modified to simplify machining processes.

Vacuum Preloaded Air Bearings

Vacuum preloaded air bearings are placed on the back side of the optic. Vacuum is used to balance the air bearing force while decreasing the air gap for better stiffness. It should be noted that although the stiffness of the bearing is bi-directional, it increases from its nominal value while pushing the optic towards the bearing, but decreases while pushing away from it.

Since a practical value of vacuum of around 414 mm of Hg (8 psi) is much less than the pressure that can be used, vacuum is placed on the outer diameter of the bearing to make use of the larger area, thus larger vacuum force.

It is preferable to use porous material for a uniform pressure distribution in the air gap; however, to properly model the flow characteristics in porous media, Darcy's Law from Equation 2.1 must be used, which utilizes the permeability of the material. Most vendors are not aware of the permeability of the porous ceramics they manufacture, which increases the complexity while decreasing the accuracy of the modeling.

To minimize optic surface slopes within the bearing region, concentric and consecutive pressure and vacuum rings must be used, as shown in Figure 4-8 such that the slope after the last ring is close to zero to reduce sine errors seen on the free ends of the optic. The detailed analysis and manufacturing of such rings is complicated and expensive, not to mention the risk of the optic stability due to a low stiffness in the direction away from the bearing.

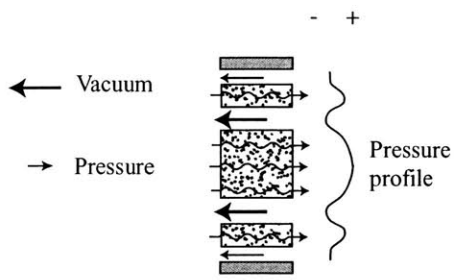

Figure 4-8: Cross-sectional view of concentric pressure and vacuum rings used to constrain the optic without introducing local torques on the optic surface.

Double-Sided, Inherently Compensated Air Bearings

This concept utilizes air bearings to constrain five degrees of freedom of the optic, as shown in Figure 4-9. Three pairs of opposing air bearings are used to constrain x translation and y and z rotation. Two vacuum preloaded air bearings are used to constrain z translation and x rotation.

One of every pair of the opposing, inherently compensated air bearings acts as a reference point, three points forming a plane. The goal is to make this plane as close to the vertical as possible to decrease deformation associated with gravity sag. These reference bearings are shown behind the optic in Figure 4-9. Because there is no contact with the optic's surface, this strategy allows for thermal expansion mismatch between optic and device while eliminating contact and non-repeatable friction forces.

4.2 Concepts

In order to evaluate the different strategies considered, a Pugh chart is formed with the most important functional requirements and design parameters, as shown in Table 4.3. The two most promising concepts for this device are the double-sided air bearings and flexures. Both concepts have been analyzed, tested, and evaluated.

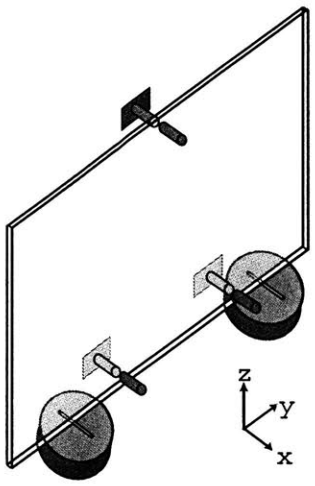

Figure 4-9: Three pairs of opposing air bearings constraining x translation and y and z rotation, and two vacuum preloaded air bearings constraining z translation and x rotation. The bearings at the front surface of the optic can be moved back and forth to facilitate inserting the optic into the device.

	Value	Double-sided bearings	Vacuum preloaded bearings	Double-sided flexures
Stiffness	3	+	+	+
Friction errors	3	+	+	+
Thermal mismatch errors	4	+	+	+
Gravity sag errors	4	+	+	+
Stability	4	+	0	+
Assembly complexity	3	-	+	-
Cost	2	-	-	+
Design complexity	2	-	-	0
Repeatability	4	+	0	+
Accuracy	4	+	0	+
Result		19	13	25

Table 4.3: Pugh chart used to select best concepts to further be developed

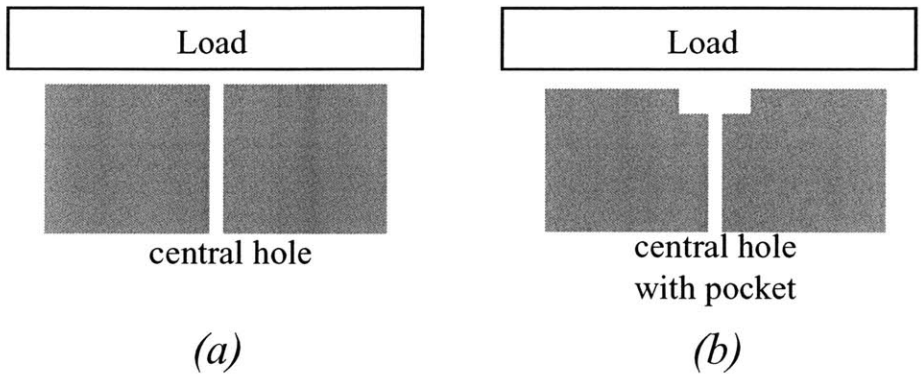

Figure 4-10: Types of air bearings: *(a)* inherent compensation and *(b)* pocket compensation

4.2.1 Double-Sided, Inherentely Compensated Air Bearings

Circular air bearings come in different configurations. Porous bearings have been thoroughly discussed in Chapters 2 and 3. The most basic types of air bearings are the inherently and pocket compensated ones shown in Figure 4-10. More complex types of bearings can be realized from these basic configurations.

Inherent compensation is achieved by drilling a narrow, long hole in the center of a circular pad to allow for air to enter the gap through the restrictor and disperse radially out towards the circumference. The pressure is highest near the center of the bearing and decreases to atmospheric at the edges. This pressure distribution eliminates any tilt resistance, which can be provided by having an annular geometry with multiple holes rather than one central hole. If the restrictor volume is made smaller than the volume in the air gap, inherent compensation reduces the possibility of having pneumatic hammer, an instability problem associated with the compressibility of gases, which leads to a continuous cycle of pressure fluctuations in the system.

Pocket compensation is achieved by either drilling a large diameter hole and press-fitting a pierced insert to a specific depth, or by making a narrow, long hole and then machining a big pocket around the hole. This type of air bearings can carry heavier loads than the inherent ones because the pressure in the pocket is close to the supply

pressure. This also allows for a better stiffness and tilt resistance; however, pocket compensated bearings are more susceptible to air instabilities due to the large volume of air in the pocket. If poorly designed, the flow can easily exit the restrictor at sonic speeds causing a huge pressure drop due to the presence of a supersonic regime afterwards.

Three pairs of opposing, inherently compensated bearings constrain three degrees of freedom of the optic without introducing errors associated with placement friction and thermal mismatch between the optic and the device. The remaining degrees of freedom are constrained using vacuum preloaded air bearings. The three opposing bearings must act as pins, each constraining translation in one direction but allowing for moments; therefore, the bearings must allow for tilt to avoid overconstraining the optic. Since the load on these bearings is minimal, and bearing instability is not acceptable, inherently compensated bearings have been chosen.

Experiments have shown that the pressure distribution in an air bearing clearance can be modeled using viscous flow relations [37]; however, it has also been noted that under certain conditions, a significant pressure drop is seen in the clearance near the inlet that can not be explained using the viscous flow equations. Various attempts have been made to understand the theory behind this sudden change in pressure, which reduces the load carrying capacity and overall stiffness of the bearing. This phenomenon, mostly observed in thrust bearings, has been attributed to the effects of inertial flow in the air gap. Mori [38] made an attempt to understand the nature of flow in the clearance by assuming that at a given pressure and air gap thickness, the flow reaches the inlet to the clearance at choked conditions. The restrictor, where air is first squeezed, and the air clearance, where the streamlines begin to diverge and the flow area increases, act as a converging-diverging nozzle with choked flow at the critical area causing the flow to enter the clearance at supersonic velocities. The pressure drop seen near the inlet to the clearance is associated with the high velocity. The supersonic flow changes to a subsonic one in the air clearance through a number of oblique and normal shock waves. At this point a static pressure recovery is observed associated with a decrease in velocity. This pressure further decreases to

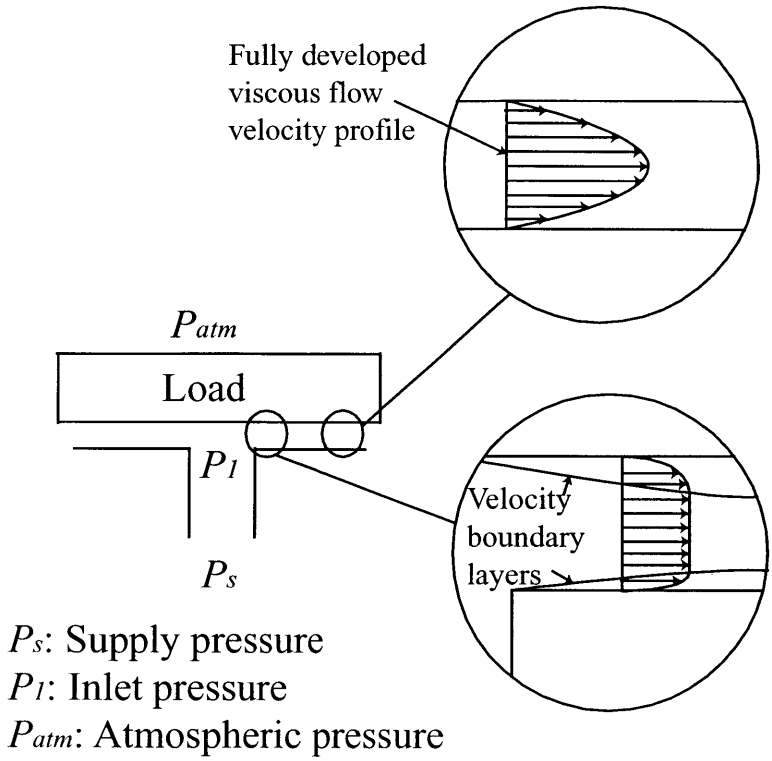

Figure 4-11: The development of boundary layers at the inlet, where flow is mostly inertial, and several air gap thicknesses away from the inlet, where the flow is purely viscous and load carrying capacities are obtained.

atmospheric as the flow reaches the periphery of the bearing. The accurate modeling of the flow under this condition is extremely complex due to the radial thickening of the boundary layers and the presence of the shock waves, which lead to the separation of the boundary layers resulting in a chaotic condition during transition.

For small air gaps, the flow in the clearance is purely viscous and isothermal with fully developed boundary layers except near the inlet, as shown in Figure 4-11. The theoretical pressure distribution in the air gap is [37]

$$P = \left(1 - \left(1 - \frac{P_1^2}{P_{atm}^2}\right)\frac{ln\frac{r}{r_2}}{ln\frac{r_1}{r_2}}\right)^{\frac{1}{2}}, \tag{4.20}$$

where P_1 is the inlet pressure to the bearing land assumed equal to the supply pressure, P_{atm} is the atmospheric pressure, r_1 is the bearing inner radius, r_2 is the bearing

outer radius, and r is the radius at any point. The film pressure exceeds atmospheric pressure and creates load carrying capacities.

As the air gap thickness increases, the flow goes through the supersonic regime. Mori [17] was the first to try to understand the theory behind the nature of this problem. In his analysis, he assumed that the properties of the adiabatic gas do not change throughout the gap length and thickness, and that the viscous drag exerted by the two surfaces is characterized by the constant friction factor f. As the streamlines approach the bearing periphery, one normal shock wave occurs to change the flow into the subsonic regime, where the flow is purely viscous with negligible inertial effects, as discussed earlier.

For supersonic flow to occur, the gas at the inlet is at the critical condition with a critical pressure P^* of $0.528P_s$, where P_s is the supply pressure. Using the momentum equation with the continuity, perfect gas, and adiabatic flow energy equations, the following first-order non-linear differential equation is obtained:

$$\left(\frac{F-k}{(k-1)(F^2-1)}\right)\frac{dF}{d\left(\frac{r}{r_o}\right)} = \frac{r_o}{r} - \frac{fr_o}{2h}\left(\frac{k}{k-1}\right)(F-1), \tag{4.21}$$

where k is the gas constant, r is the radius from the inlet of the bearing, r_o is the restrictor radius, f is the friction factor, h is the air gap thickness, and F is a function of r and P defined as

$$F \equiv \sqrt{1+(k^2-1)\left(\frac{{r_o}^2}{r}\right)\left(\frac{{P^*}^2}{P}\right)}. \tag{4.22}$$

The exact solution of Equation 4.21 is not known; however, a first order approximation assuming the friction factor f to be zero can be easily obtained and solved. At $r = r_o$, where critical conditions prevail, $F = k$. Therefore the solution of Equation 4.21 for a frictionless case is

$$\left(\frac{r_o}{r}\right)^2 = \left(\frac{k+1}{k-1}\right)\left(\frac{P}{P^*}\right)^{2/k} - \left(\frac{2}{k-1}\right)\left(\frac{P}{P^*}\right)^{(k+1)/k}, \tag{4.23}$$

which governs the pressure profile shown in Figure 4-12 in the bearing clearance for a pure supersonic flow.

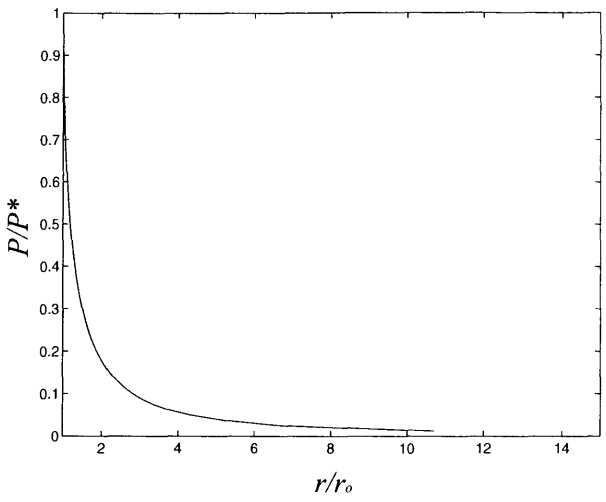

Figure 4-12: The pressure profile P of a purely supersonic flow in the air bearing clearance at a distance r from the center of the bearing, where P^* represents the critical pressure at the inlet orifice of radius r_o.

Once the shock wave occurs, static pressure is recovered and the velocity of the flow is reduced. As the position of the shock wave moves further from the inlet hole, the associated pressure recovery decreases; therefore, in order for the bearing to maintain load carrying capacities, the shock wave position should be close to the inlet to allow for a pressure-differential viscous flow. To avoid having sonic flow at the entrance to the air gap, it is recommended to reduce the working pressure and air gap thickness.

The performance of an air bearing highly depends on the air film thickness. These air bearings are to be placed against the optics measured, which in turn have a characteristic surface warp. The bearing outer diameter is calculated, as shown in Figure 4-13, such that the air film thickness variation due to the surface non-flatness of the optics is limited to 3 μm. The optic has a large radius of curvature R with an original warp of 25 μm, a value typical for silicon wafers. From the geometry of the figure, the following equations are obtained

$$\delta = R(1 - cos\theta) \tag{4.24}$$

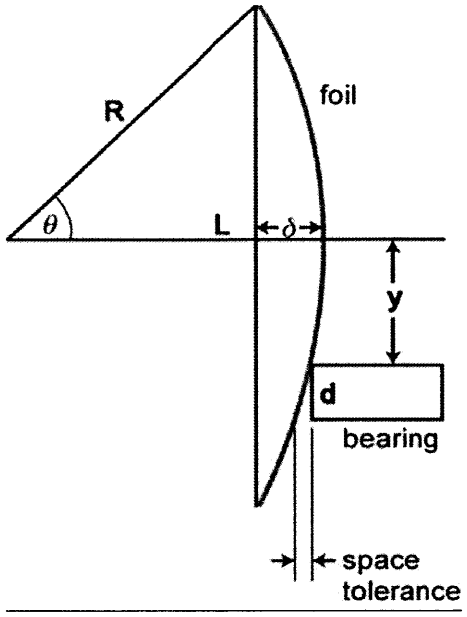

Figure 4-13: Optic modeled with a curvature δ in order to calculate the bearing diameter d for a gap variation of 3 μm

$$sin\theta = \frac{L}{2R}, \tag{4.25}$$

where θ is the half-angle, δ is the optic warp, and L is the characteristic length. For small angles $\theta = \frac{L^2}{8R}$. For a distance $y = 45$ mm away from the center of the optic, the bearing diameter d is 6.53 mm. An outer diameter of 7 mm is chosen. Since this diameter is rather small compared to typical values, several factors must be taken into consideration when optimizing the performance of these bearings. The flow in the air film must be fully developed viscous at pressures higher than ambient for the bearing to have a load carrying capacity. It has been shown [38] that increasing the ratio of the inner against the outer diameters of the air bearings decreases entrance effects such as separation and frictional losses caused by changes in flow direction; however, this leads to a decrease in flow resistance, which in turn leads to a drop in stiffness. The inner diameter is chosen to be 0.4 mm (a practical value to achieve in the machine shop) to give an inner to outer diameter ratio of 0.057, which is close to the commonly used ratio of 0.05 [11].

The feeding parameter Λ is defined as the ratio of the resistance to flow presented by the restrictor to the resistance to flow presented by the thin air film carrying the load. Experimental results show that the stiffness of an inherently compensated air bearing is a maximum when $\Lambda = 0.85$ [11].

$$\Lambda = \frac{126.2 r_o}{P_s h^2} ln \frac{R}{r_o}, \tag{4.26}$$

where r_o is the radius of the restrictor, P_s is the absolute supply pressure, h is the air gap thickness, and R is the bearing outer radius. The peak value of stiffness shown in Figure 4-14 is equivalent to having the ratio of outer to inner bearing diameters equal to 0.05. Although the stiffness at this point is a maximum, this may not be the optimal region of operation, where the change in stiffness due to small gap variations is minimal. Stiffler [39] proved that maximum stiffness for inherently compensated bearings is obtained in the unstable operating range at the expense of damping. Another good design criterion is to have the inlet flow area at least twice the curtain flow area [11]

$$\frac{\pi r_o^2}{2\pi r_o h} = \frac{r_o}{2h} > 2. \tag{4.27}$$

To facilitate the use of these bearings, it is required that the air gap thickness not be less than 9 μm. Replacing $R = 3.5$ mm, and $r_o = 0.2$ mm into Equation 4.26, a relation between the supply pressure and air gap thickness for a given feeding parameter is found to be

$$P_s = \frac{72.24}{\Lambda h^2}. \tag{4.28}$$

For a gap of 10 μm and a feeding parameter of 0.85, the absolute supply pressure is found to be 0.85 MPa, which is equivalent to 123 Psi. This pressure value is extremely high, and it would be associated with bearing instability and a large pressure drop due to supersonic flow even at small gaps. Therefore, the feeding parameter had to be iterated with varying air gaps to come up with the final design supply pressure. For a feeding parameter of 1.5 and an air gap of 11 μm, the absolute pressure is

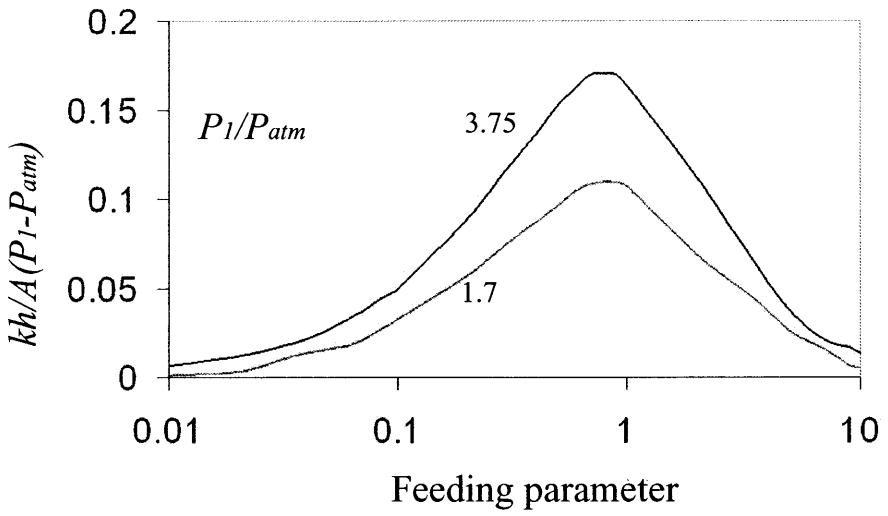

Figure 4-14: Plot of non-dimensional stiffness versus air bearing feeding parameter. Stiffness is maximum when feeding parameter is 0.85 [11].

found to be 0.39 MPa, which is equivalent to 57 Psi or a gauge pressure of 42.5 Psig. Replacing $h = 11$ μm in Equation 4.27 with $r_o = 0.2$ mm, the ratio is found to be approximately 9, which meets the design criterion.

Figure 4-15 shows the pressure distribution in the viscous film as a ratio of pressure P to supply pressure P_s for a 7 mm diameter bearing with a 0.4 mm diameter orifice. For a supply pressure of 0.276 N/mm^2 (40 Psig), the theoretical load capacity W is 3.1 N calculated using [37]

$$\zeta = \frac{W}{P_{atm}\pi r_2^2} = \frac{P_1}{P_{atm}}\frac{r_1^2}{r_2^2}e^{\frac{2}{a}}\sqrt{\frac{\pi a}{8}}\left[erf\left(\sqrt{\frac{2}{a}}\right) - erf\left(\frac{P_{atm}}{P_2}\sqrt{\frac{2}{a}}\right)\right] \tag{4.29}$$

$$a = \frac{1 - \frac{P_{atm}^2}{P_1^2}}{ln\frac{r_2}{r_1}}. \tag{4.30}$$

Figure 4-16 shows the experimental setup for the double-sided air bearings. To facilitate the placement of the optic into the device, one of the opposing air bearing pair must be pulled back to create an opening. After the optic is in place, the

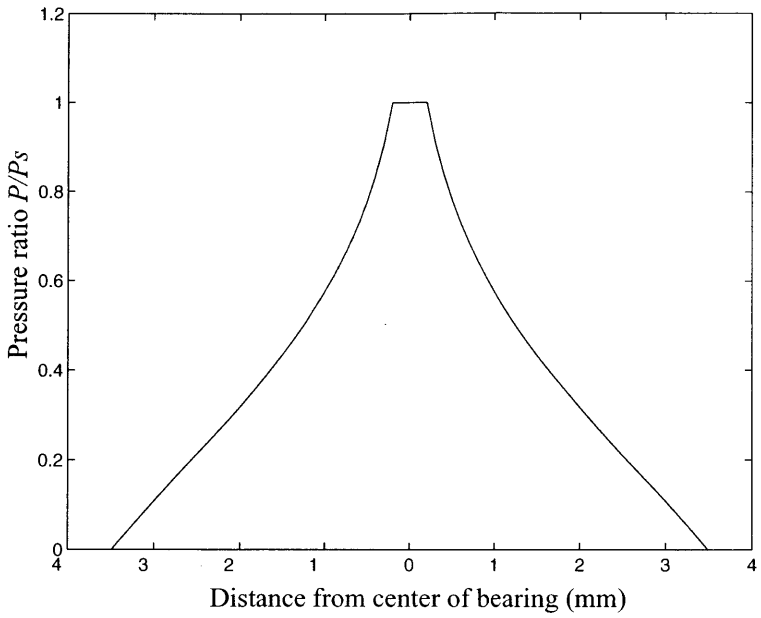

Figure 4-15: Pressure distribution for a fully developed viscous flow of a 7 mm diameter air bearing with a 0.4 mm orifice.

retracted bearing of each pair must be moved back toward the optic to fully constrain it repeatably. As the bearing approaches the optic, the resulting force changes from jet impact to supersonic to finally viscous force. A balance between the actuation force and the viscous force is the key parameter in the repeatable placement of the bearing with respect to the optic.

The shaft of the moving bearing is carried by means of a journal air bearing to eliminate non-repeatable friction forces. Air pressure is used to actuate the shaft on one end, and a second pressure source is used to feed the air bearing on the other end. Since connection lines introduce non-repeatable forces into the set up, the bearing pressure source must not be attached to the moving shaft.

The actuation force acting on the shaft causes the bearing to come in contact with a reference stationary surface, where a capacitance probe is attached to constantly measure the gap between the bearing and the stationary surface. As the air bearing is moved towards the reference body, it goes through the supersonic regime leading to a negative load capacity, which causes the shaft to collapse onto the body. Therefore,

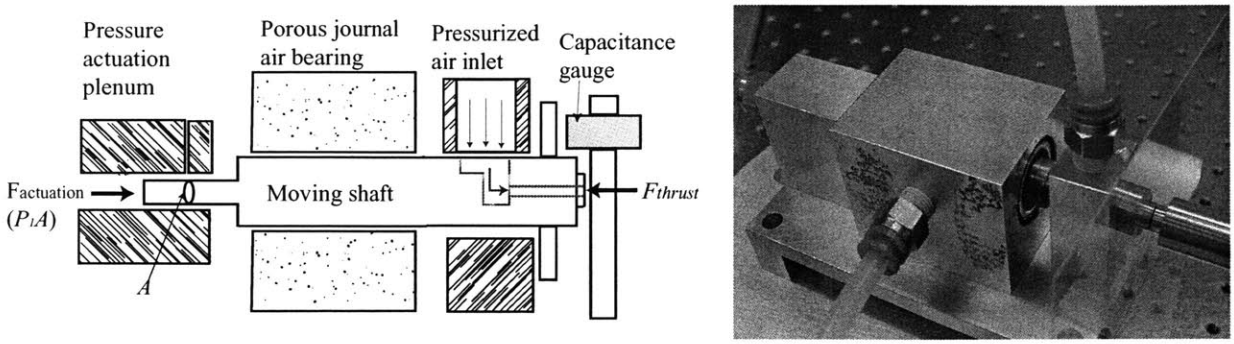

Figure 4-16: Experimental setup for the double-sided air bearing. The thrust force of the moving bearing is balanced by the actuating force on the opposite end of the bearing shaft. A capacitance gauge is used to calculate the gap between the air bearing and the reference surface. A force-gap curve is formed to assist in the proper positioning of the air bearing with respect to the thin optics during metrology. The figure on the right shows the double-sided air bearings constraining the top of a thin optic.

the shaft has to be brought into contact with the body using the actuation pressure, a reference reading taken and the air bearing pressure turned on. The resulting thrust force causes the shaft to move backward until a balance between bearing and actuation forces is achieved. The thrust of the bearing decreases with increasing distance from the reference body. This test is conducted for different actuation forces and a curve is calibrated for every bearing pair. During metrology of thin optics, this curve, shown in Figure 4-17, is used to place the bearing at a proper distance from the optic using the actuation force. The overall displacement of the shaft is on the order of a few millimeters.

It is important to avoid the presence of local refrigeration effects on the optic due to the cooling of the emerging air. The two major reasons why air temperature drops are high velocity and change in volume. As the velocity of a compressible fluid increases, its enthalpy drops, and this is associated with a drop in temperature. Since the flow rate in air bearings is extremely small, air can be modeled as an incompressible medium, where a change in velocity is independent of change in enthalpy, and thus

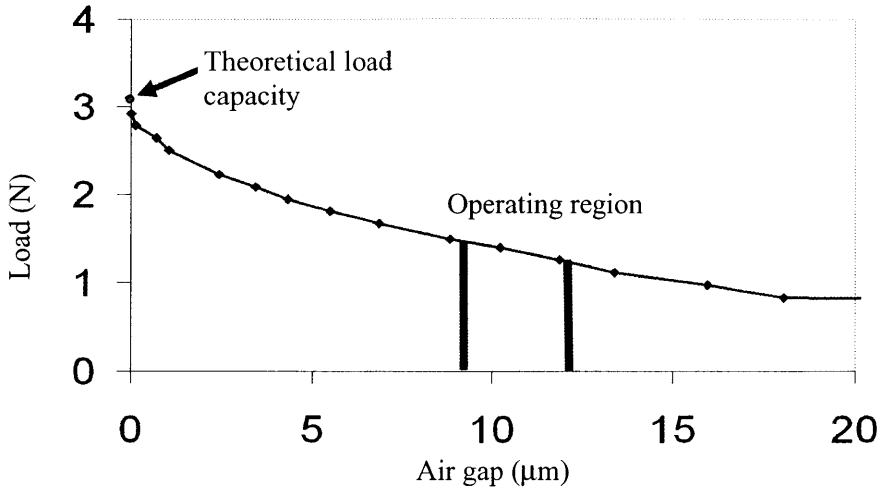

Figure 4-17: Plot of the force a bearing exerts at different gaps between the bearing and the constrained surface.

a drop in temperature. Also, as a compressed gas at high pressures is allowed to go through a throttle to expand at lower pressures, its temperature drops. This is known as the Joule-Thompson effect for real gases, where the Joule-Thompson coefficient at constant enthalpy h is defined as

$$\left(\frac{\partial T}{\partial P}\right)_h = \frac{1}{c_p}\left[T\left(\frac{\partial \nu}{\partial T}\right)_p - \nu\right] = \mu_{JT}, \tag{4.31}$$

where μ_{JT} is the Joule-Thompson coefficient, T is temperature, P is pressure, ν is specific volume, and c_p is the specific heat at constant pressure, which equals 29.1 J/mole.K [40]. Using the van der Waal equation of state for real gases given by

$$\nu = \frac{RT}{P} + b - \frac{a}{RT}, \tag{4.32}$$

where $R = 83.14$ J/mole.K is the universal gas constant, and a and b are the Van der Waal constants for the gas concerned, the coefficient μ_{JT} is

$$\mu_{JT} = \left(\frac{\partial T}{\partial P}\right)_h = \frac{1}{c_p}\left(\frac{2a}{RT} - b\right). \tag{4.33}$$

For air, $a = 0.1361$ Jm^3/mole^2 and $b = 3.85 \times 10^{-5}$ m^3/mole, which gives a value of 1.89×10^{-6} K/Pa for the Joule Thompson Coefficient. Therefore, for a pressure drop of 40 Psig=275,862 Pa, the resultant temperature drop is 0.52K. However, this model does not take the viscous heating effects into consideration. In reality, experiments conducted by Grinnell (1956) and Comolet (1957) [37] have shown that the air film is isothermal, where cooling effects are compensated for by viscous heating effects. In addition, using a metallic surface for the air bearings assures that the heat change is absorbed by the metal rather than the optic.

This non-contact design eliminates Hertzian contact stresses and deformation, while providing a preload force to hold the optic with an acceptable stiffness, without distorting its free-surface. The major problem with this concept is the numerous connection lines to the device to supply the air pressure. The design requires tight tolerances, which increase the time of manufacturing and raise the price and complexity of the overall assembly.

4.2.2 Double-Sided Monolithic Flexures

An alternative, passive design utilizes three double-sided flexures contacting both sides of the optic. The primary candidate for these flexures is stress-relieved aluminum 6061 T651 for its high yield stress to Young's modulus ratio, ease of machining, availability, and low cost. Several designs have been considered with different sizes.

Monolithic flexures have been chosen to constrain the optics to minimize misalignment between the opposing flexures, where both are machined in one step using wire-electric-discharge machining (wire-EDM). The monolithic structure is divided into two sets of flexures, as shown in Figure 4-18.

The vertical flexure allows for one arm of the flexure module to open while inserting the optic, and it provides a preload once the optic is in proper position, and the extended arm is released. The opposing flexures account for thermal expansion mismatch between the optic and the device.

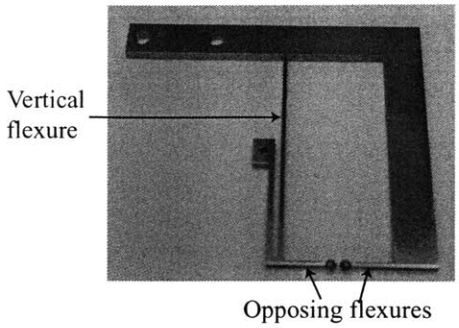

Figure 4-18: Monolithic, wire-EDM-ed, double-sided flexures made of stress-relieved aluminum 6061 T651 with ruby ball tips. The left vertical arm is actuated back and forth from its center to allow for the optic insertion/removal. The opposing flexures accommodate thermal expansion mismatch between the optic and the aluminum device.

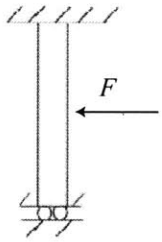

Figure 4-19: Vertical flexure modeled as a beam with one fixed end and one guided end, and with a force acting at the middle of the flexure length.

Vertical Flexure Arm

The vertical flexure is designed to have a horizontal displacement of 1.6 mm with a maximum stress of 145 MPa, which corresponds to 52% of the yield stress of aluminum. This large deflection is needed when inserting the optic between the opposing flexures. The vertical flexure, actuated at its midpoint, is modeled as a beam with an upper fixed end and a lower guided end, as shown in Figure 4-19. The lateral stiffness is [41]

$$k = \frac{12EI}{L^3}, \tag{4.34}$$

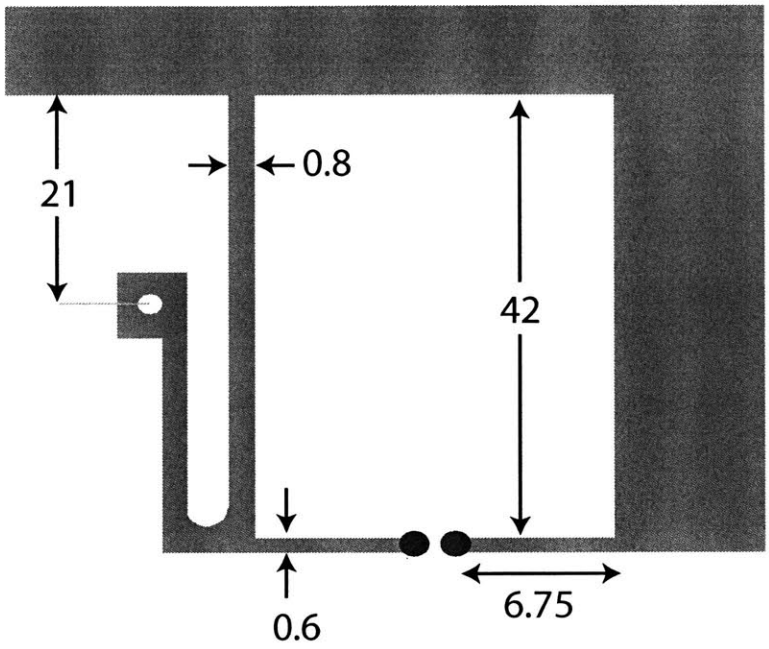

Figure 4-20: Monolithic flexure dimensions in mm. The width of the flexure is 2 mm into the page. The ruby balls at the opposing flexure tips are 2 mm in diameter.

where k is the lateral stiffness, E is Young's modulus, I is the moment of inertia, and L is the length of the flexure. For the dimensions shown in Figure 4-20, the vertical flexure has a lateral stiffness of 9.8×10^{-4} N/μm. This flexure is actuated at its midpoint to minimize parasitic vertical motions associated with lateral deflections [11]. The tip of the vertical flexure undergoes very small parasitic motion; however, the free end of one of the the opposing flexure pair attached to the vertical arm undergoes a larger parasitic motion due to a sine error. This places an upper limit on the length of the opposing flexures, if misalignment between them is to be kept at minimum. Upon removing the actuation force from the vertical arm, it springs back until contact with the optic is achieved. At this point the flexure acts as a cantilever with a stiffness of 2.45×10^{-4} N/μm, calculated using Equation 4.18.

Upon placing the 0.4 mm thick optic into the device, the vertical arm is displaced by 275 μm, which corresponds to a force of 0.067 N. The fact that this preload force is small poses a risk on the overall stability of the device. Tests have shown that this does not manifest itself as a problem, and the optic does not vibrate while constrained;

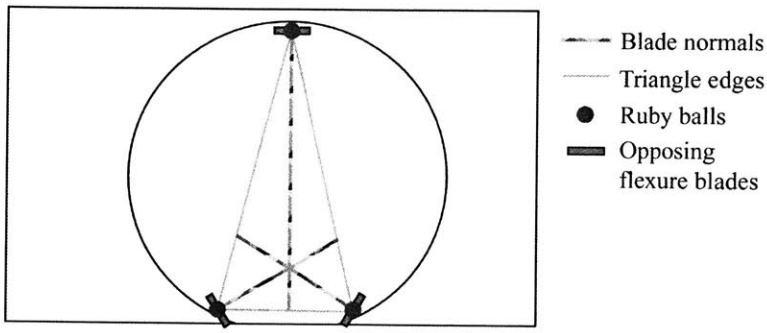

Figure 4-21: Flexure blades placed such that the normals to these blades bisect the angles of the triangle formed by the three contact points between the optic and the ruby balls. The figure shows overlaid circular and rectangular optics.

however, the countermeasure is to resize the dimensions to increase the stiffness of the vertical flexures resulting in a smaller opening during optic insertion/removal.

Opposing Flexure Arms

Blade flexures are compliant in only one direction, whereas thermal expansion occurs in all directions; therefore, the blade flexures must be held at different angles for best stability and performance. The flexures are placed such that the normals to the blades of the flexures bisect the angles of the triangle formed by the three contact points with the optic, as shown in Figure 4-21. This is analogous to the kinematic coupling lay out for best stability, where the couplings constrain the carried load in all directions [11]. The top flexure is the most susceptible to thermal mismatch errors because the differential length between the optic and the device is a maximum at this point; therefore the blade of the top flexure is placed such that its compliance is along the direction of maximum thermal growth.

The tips of the opposing flexures have a post used for mounting drilled, 2 mm diameter ruby balls. Contact occurs between the ruby balls and the optic. Ruby is chosen for its hardness, which implies better repeatability and smaller Hertzian deformation δ_{Hz} given by

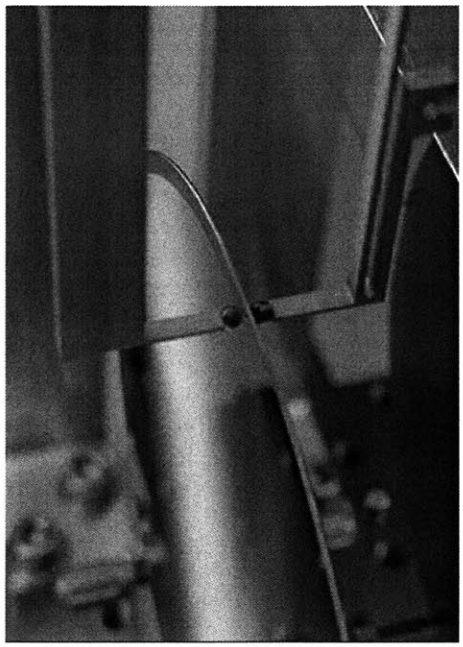

Figure 4-22: The constraint of a silicon wafer with 400 nm spatial period grating by the monolithic flexure with two ruby balls mounted at the tip of the opposing arms

$$\delta_{Hz} = \frac{1}{2}\left(\frac{1}{R_{eq}}\right)^{1/3}\left(\frac{3F}{2E_{eq}}\right)^{2/3}, \tag{4.35}$$

where R_{eq} and E_{eq} are the equivalent radius and Young's modulus given by Equations 4.15 and 4.14, respectively, and F is the preload force of 0.067 N at each contact point. The resulting optic deformation on each side is 76 nm; however, the Hertzian forces are on opposite sides of the optic, cancelling each other out and diminishing their effect on the overall shape of the optic. Figure 4-22 shows a silicon wafer with 400 nm period grating diffracting white light while being constrained by the two ruby balls.

When calculating the required lateral stiffness for the horizontal flexures, it is assumed that the point of contact between the ruby ball and the optic, after the flexure mechanism preloads both sides of the optic, does not allow for slip. The flexures are modeled as cantilevers. An upper limit of 1°C temperature change per reading determines the amount of flexure deflection needed. For a coefficient of friction of 0.3 between ruby and glass [33], and a preload of 0.067 N, the corresponding

friction force is 0.02 N. The flexures are located at characteristic thermal lengths of 100 and 17 mm. For a 1°C temperature variation, the differential changes in length between the aluminum housing and silicon optic at both positions are 1.2 and 0.27 μm, respectively. These values correspond to the displacement at the flexure tip caused by the friction force calculated previously. Therefore, the required stiffness k ranges between 0.017 and 0.095 N/μm. To minimize the parasitic motion shown in Figure 4-23, a length of 6.75 mm is chosen for all opposing flexures with a thickness of 0.6 mm for ease of machining, which gives a stiffness of 0.024 N/μm.

The flexure placed at the critical length of 100 mm is not as compliant as it must be in order for it to bend and accommodate the 1.2 μm difference. The friction force of 0.02 N would only cause the flexure to bend by 0.8 μm; however, the aluminum housing would have expanded by the additional 0.4 μm. This results in a net axial force along the length of the optic. The stiffness of the optic k_{optic} along the vertical direction when modeled as a beam is

$$k_{optic} = \frac{EA}{L}, \tag{4.36}$$

where E is Young's modulus, A is the cross-sectional area, and L is the length of the optic. For the rectangular optics, the stiffness is 39.2 N/μm; the optic is infinitely stiff compared to the flexures. Therefore, the axial force caused by the thermal expansion of the aluminum housing will cause the flexures to bend before the effect is transmitted to the optic. As the flexure further bends, the restoring force at its tip becomes larger than the static friction force at the interface between the ruby ball and the optic, and the flexure tip slips along the optic. For these flexures to function properly, the maximum stress at the base must not exceed 50% the yield stress of aluminum. For the overestimated 1.2 μm displacement of the flexure, the resulting force at the tip is 0.029 N. For the 6.75 mm length chosen, the moment at the base of the flexure is 1.944×10^{-4} Nm. The maximum stress σ_{max} is at the surface of the blade and equals

$$\sigma_{max} = \frac{Mh}{2I}, \tag{4.37}$$

Zernike Coefficient	Z20	Z21	Z22	Z30	Z31	Z32	Z33	Z40	Z41	Z42	Z43	Z44
Maximum Variation (nm)	47.5	29.5	45	24	23	15.5	25	9	10.5	5	13.5	15.5

Table 4.4: Maximum variation in Zernike coefficients during a span of 3 hours, where the temperature increases by 1.2°C

where M is the moment applied, h is the thickness of the blade, and I is the moment of inertia. For the dimensions chosen, the maximum stress is 1.62 MPa, which corresponds to 0.6% of the yield stress of aluminum.

Measuring the surface of an optic over a period of 3 hours, during which the temperature of the room increases by 1.2°C reveals a maximum change of 47.5 nm in the second order Zernike polynomial. This is the largest deviation seen in the polynomials as anticipated; however, these polynomials have a static repeatability of approximately 30 nm over a period of <5 minutes. Table 4.4 summarizes the maximum change in the Zernike polynomials during the 3 hour span.

FEA is used to determine the parasitic motion associated with the displacement of the flexure, which is found to be 6.6 μm, as shown in Figure 4-23. To see the effect of this displacement, the optic is modeled as a simply-supported beam with twin loads at a distance of 6.6 μm away from the supports, as shown in Figure 4-24. The maximum deflection δ is [42]

$$\delta = \frac{Fa(3L^2 - 4a^2)}{24EI}, \tag{4.38}$$

where F is the preload, a is the parasitic displacement, L is the distance between the top and bottom flexures, which equals 91.7 mm, E is Young's modulus, and I is the moment of inertia. The corresponding maximum deflection is 8.65 nm. This value is insignificant when compared to other major sources of errors in both the device and the metrology tool.

The lateral stiffness of these blade flexures controls the stability of the optic during metrology. The optic is constrained by two identical flexures on opposite sides with

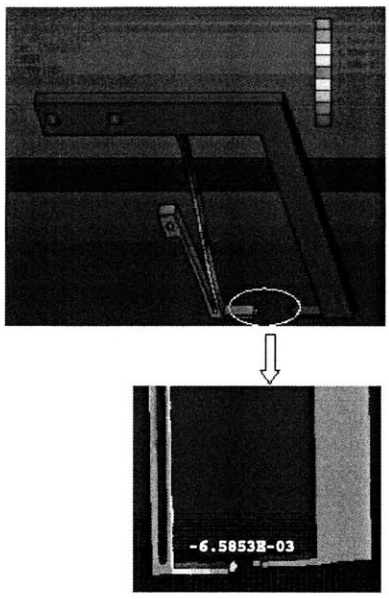

Figure 4-23: FEA of flexure arms after optic insertion. The top figure shows a lateral displacement of 0.275 mm due to placing the 0.4 mm thick optic between the two arms, with the associated vertical parasitic displacement of 6.6 μm between the opposing flexures shown in the lower figure.

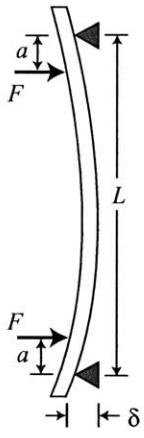

Figure 4-24: Thin optic modeled as a simply-supported beam with twin loads to characterize the deflection δ caused by the misalignment of the ruby balls due to the parasitic motion. F is the preload of the flexure on the optic, a is the parasitic displacement, and L is the distance between the upper and lower monolithic flexures.

an axial stiffness $k = EA/L$. For the dimensions chosen, this stiffness is 12.62 $N/\mu m$. The effective stiffness, however, is also determined by the stiffness of the vertical arm $k_{vertical}$ of this monolithic flexure, which is in series with one of the arms of the attached opposing flexure stiffness $k_{opposing}$; therefore, the equivalent stiffness k_{ev} of these two flexures is given by

$$k_{ev} = \frac{k_{vertical} k_{opposing}}{k_{vertical} + k_{opposing}}. \tag{4.39}$$

The opposing-pair stiffness $k_{opposing} = 12.62$ N/μm along its axis and is much larger than the vertical arm bending stiffness $k_{vertical} = 2.45 \times 10^{-4}$ N/μm. The resulting k_{ev} is 2.45×10^{-4} N/μm. The effective stiffness k is the sum of $k_{opposing}$ and k_{ev}.

Load Carrying Flexures

To remove the effects of friction and thermal expansion while supporting the weight of the optic, "antenna" flexures are used to constrain the remaining three degrees of freedom. Four flexures are present to accommodate different optic sizes, but only two are in contact with a given optic, as shown in Figure 4-25. The two inner flexures in the middle are 0.5 mm shorter than the two external ones. This allows the flat on the circular optics to be placed on the inner pair, whereas wider, rectangular optics are placed on the outer, longer pair separated by a distance of $0.577L$, L being the length of the optic, for minimal gravity sag [32]. Each flexure is mounted on a linear stage that allows it to move back and forth to accommodate different substrate thicknesses. The optic sits on a hollow, 2 mm long sapphire cylinder mounted at the tip of these flexures, as shown in Figure 4-26. This creates a small line contact at the interface between the flexure and the thin foil. An identical flexure is used to constrain the side of the optic.

While placing the thin sheet into the device, a temporary torque may be applied onto the foil by the user. The resulting internal elastic force of the optic would cause it to go back to its natural shape; however, the friction force at the interface may hinder this restoring force; if this restoring force is larger than static friction, the

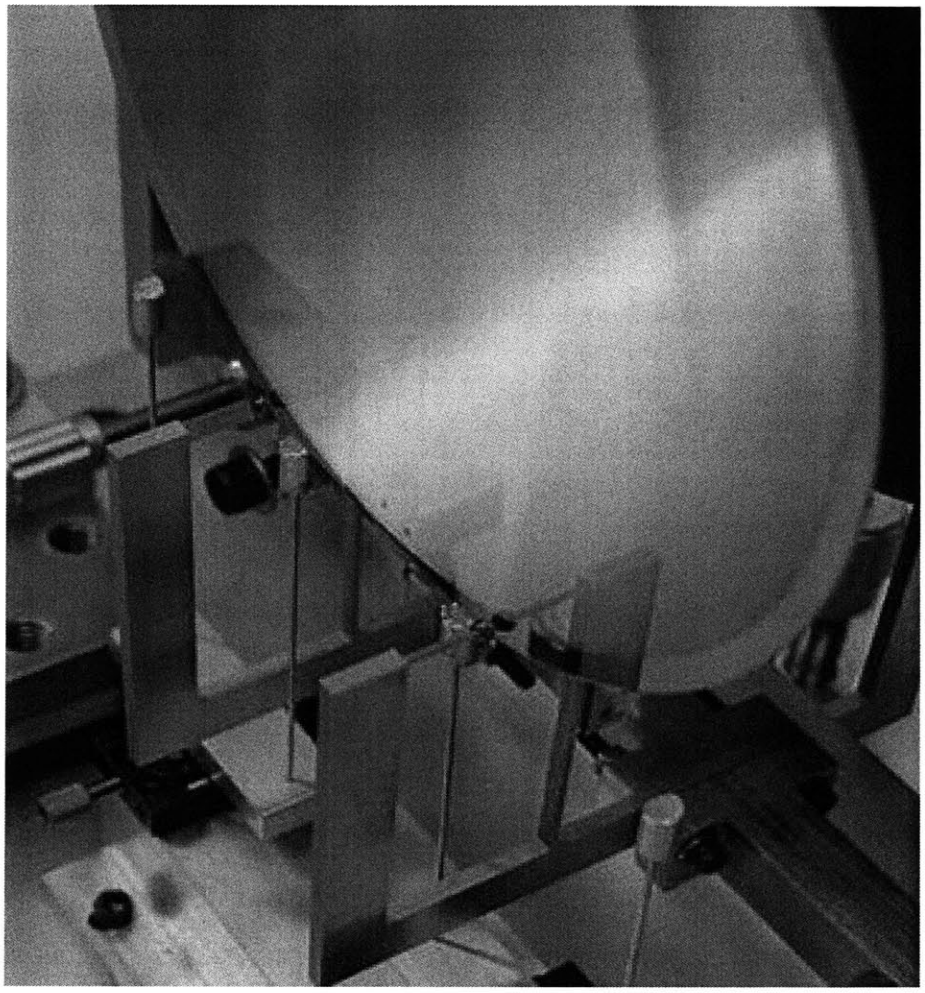

Figure 4-25: Circular optics sit on the inner pair of antenna flexures, whereas rectangular ones contact the outer, longer pair. This configuration allows for better stability with the rectangular optics, since the corresponding flexures are placed further apart; the length of the flat on circular optics (around 31 mm) constrains the distance between the inner flexures.

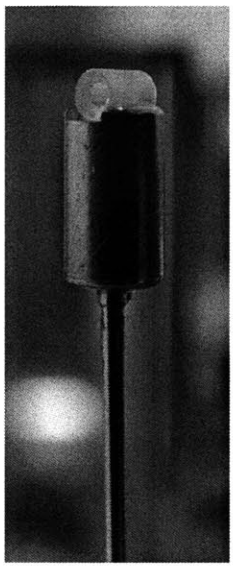

Figure 4-26: Hollow sapphire tube mounted on top of the antenna flexures to facilitate the placement of the optic on these flexures.

optic edge would slip on the constraining object, but if it is smaller than the friction force, the result is an artificial surface warp of the thin substrate during metrology.

The role of the flexure is to reduce the effects of this friction force, which is calculated to be 0.024 N using the weight of the optic, 0.138 N, equally divided between two flexures, and the coefficient of static friction between the glass foil and the sapphire tube [33]. Since the free motion of the optic is restrained by the two ruby balls, the spacing between these two balls while placing the optic into the device plays an important role on the design of the antenna flexures. The balls can be separated by 1.6 mm before a critical stress is reached in the vertical flexures as discussed earlier. The design opening distance is set to 1.3 mm. The maximum distance that the optic can move after being placed is governed by this opening gap, the initial spacing of 0.125 mm between the ruby balls before pulling one away, and the thickness 0.4 mm of the optic. Therefore, the maximum distance d_{max} is 1.3+0.125-0.4=1.025 mm.

Modeling the restoring force of the optic with different initial boundary conditions imposed by the user is difficult. The problem arises when this force is smaller than static friction, which will be used to set an upper limit on the required stiffness of the

antenna flexures. If the optic has a high enough initial torque that its restoring force forces it to cover the maximum distance d_{max}, the required stiffness of the flexure for this force is 2.36×10^{-5} N/μm.

The antenna flexures must carry the load of the optics. Rectangular optics have a load of approximately 0.14 N; however, thicker, flat mirrors weighing approximately 0.6 N must be used to align the plane of the optic with the plane of the reference block as discussed in the next section. Hollow flexures made of stainless steel are used for their availability in the form of precision tubes. The flexures are 50 mm long with an outer diameter of 0.635 mm and inner diameter of 0.508 mm. Using Equation 4.18, the actual stiffness is 2.18×10^{-5} N/μm. This value is slightly smaller than the upper limit stiffness value determined previously. To calculate the load capacity of these antenna flexures, Euler's beam buckling theorem from Equation 4.19 is used. For these dimensions and a Young's modulus of 193 GPa, the load capacity of these flexures is found to be 0.82 N, which is greater than the weight of the 1.6 mm thick flat mirrors. The maximum stress at the bottom of these flexures must not exceed 50% the yield stress of cold worked stainless steel, which is 241 MPa. The associated maximum displacement at the tip of the flexure is 1.64 mm, which is more than the 1.025 mm possible for this design.

Another factor that must be taken into account is the placement position of the optic with respect to the stationary ruby ball. The vertical arm of the monolithic flexure moves the optic towards the stationary ball. During this process, the load carrying antenna flexures would deflect and impose a spring force on the optic. Figure 4-27 shows the worst case, where the optic is placed at the very edge of the 2 mm long sapphire tube. The distance that the optic has to cover before coming in contact with the stationary ruby ball is 1 mm, since only half the length of the sapphire is actually used.

To calculate the warp induced on the optic due to the finite stiffness of the antenna flexures, the optic is modeled as an overhung, simply-supported beam with a force equivalent to $2F$ at one free end, where F is the force from a single flexure. This force is a maximum when the flexure has covered the maximum distance of 1 mm.

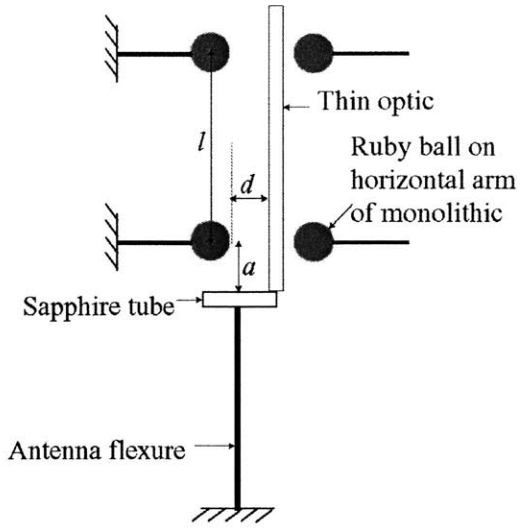

Figure 4-27: Thin optic placed at the very edge of the sapphire tube on the antenna flexures. This leads to the motion of the flexures by distance d until the optic is fully constrained, resulting in a restoring spring force from the antenna flexures onto the optic.

Therefore, for flexure stiffness of 2.18 N/μm, the corresponding force is $F = 2 \times 2.18 \times 1000 = 0.044$ N. The maximum deflection δ_{max} caused by this force is given by

$$\delta_{max} = \frac{Fa^2(l+a)}{3EI}, \tag{4.40}$$

where F is the force applied, a is the distance between the force and the closest pin, in this case 2 mm, l is the spacing between the two pins and equals 93.4 mm, E is Young's modulus and I is the moment of inertia. The maximum deflection is estimated to be 148.55 nm.

Upon placing the optic into the device, such that the flexures are moved by approximately 1 mm from their nominal position, the optic surface topography changes by an overall peak to valley value of 94.55 nm. Table 4.5 shows the corresponding changes in the Zernike polynomials. The most prominent change is in the second order polynomial, which represents the change estimated by the analytical model.

To further evaluate the performance of the antenna flexures, a glass optic is intentionally deformed (twisted), placed on the antenna flexures and released, allowing

Zernike Coefficient	Z20	Z21	Z22	Z30	Z31	Z32	Z33	Z40	Z41	Z42	Z43	Z44
Variation (nm)	-50.5	-24.5	-157.5	-0.5	1	-43.5	-49	4.5	2.5	-3	0.5	-33.5

Table 4.5: Variation in Zernike coefficients due to motion of load carrying flexures by 1 mm

Zernike Coefficient	Z20	Z21	Z22	Z30	Z31	Z32	Z33	Z40	Z41	Z42	Z43	Z44
Variation (nm)	41.27	7.5	134	1	-12.5	19	39	-5.5	-7.5	-2	2.5	32

Table 4.6: Variation in Zernike coefficients due to optic deformation before placement onto load-carrying flexures

it to spring back to its natural shape. At this point, the antenna flexures have moved while the optic is restoring to its shape. However, as the ruby balls are approached to fully constrain the optic, the flexures are forced to move back to their original position, thus inducing a force on the foil. This process is a combination of both misplacing the optic away from the centerline of the flexures and deforming it due to the flexure spring force. The overall peak to valley change in the surface topography of the optic is 119.4 nm. Table 4.6 shows the associated changes in Zernike polynomials.

The placement repeatability of the system, where an optic is placed on the load-carrying flexures, fully constrained with the ruby balls, removed and placed into the device again is 55 nm, which is very close to the repeatability of 35.6 nm of the metrology tool. This is sufficient to verify foil manufacturing and shaping processes and assure a surface non-flatness of <500 nm as required for the x-ray optics.

Vertical Alignment

To remove the effects of gravity, the optic must be held vertically within 70 arcsec, which corresponds to a surface sag of 50.4 nm [29] for a flat substrate. By placing

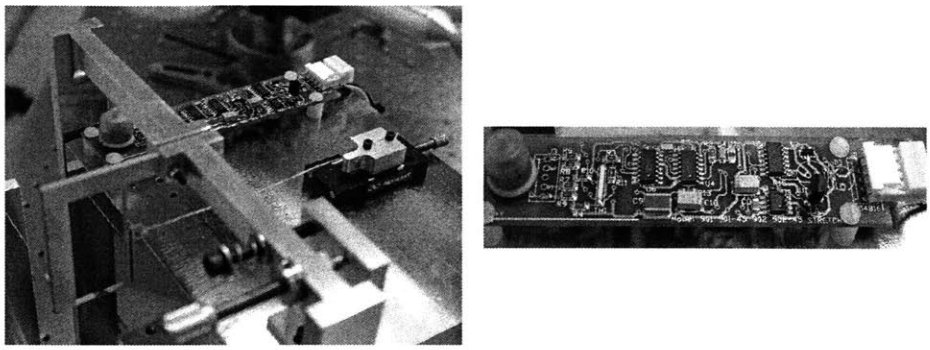

Figure 4-28: Inclinometer mounted on top of the reference flat block to monitor the change in pitch and yaw of the tool during metrology.

a rectangular sheet into the device, measuring its surface, removing and rotating it by 90°, measuring the surface again and comparing it to the initial measurement, the vertical plane can be established. At a given angle of inclination, gravity force causes a distortion along a length L. As the rectangular optic is rotated, the positions of the constraints or the boundary conditions change with respect to the optic area and material properties along given directions, and the length L changes, leading to a different gravity sag according to Equation 4.1. This difference in deformation is eliminated once the optic is in the vertical plane.

A reference block made of nickel coated aluminum with a front surface optically polished to 100 nm is used as a reference reading to compare the surface of the test optics to. This block sits on a tilt stage with three fine-threaded (1/4-100) screws used to change the pitch and yaw of the device. An inclinometer with a resolution of 18 arcsec and a repeatability of 36 arcsec in pitch and yaw, as shown in Figure 4-28, is mounted on top of the reference block to monitor the change in angle of the device during metrology.

Flexure Tilt Stage

During metrology, it is desired to have the optic front surface parallel to the surface of the reference block. This eliminates the need to adjust the beam of the Shack-Hartmann metrology system, such that the final image lands at the right position

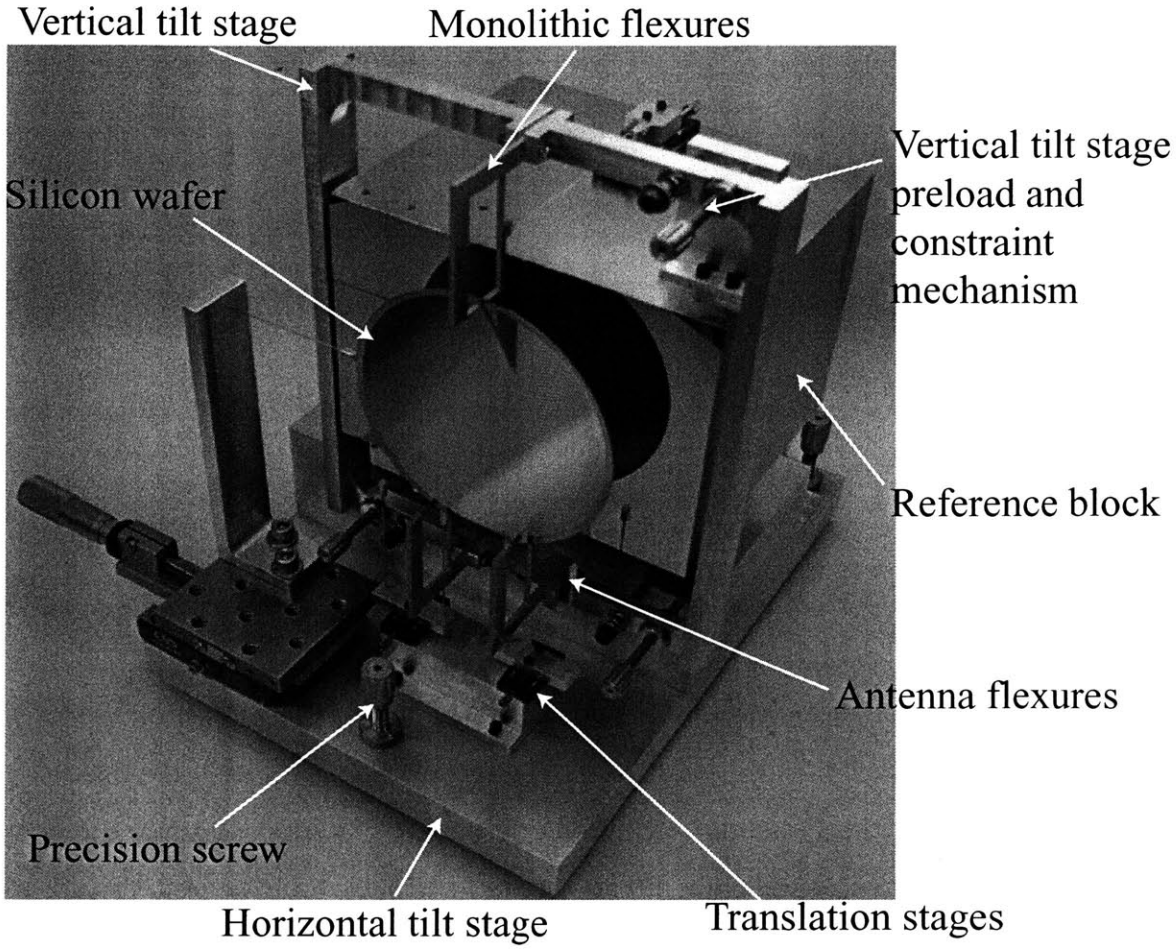

Figure 4-29: The Metrology Truss utilizing double-sided and antenna flexures to constrain a circular silicon optic during surface metrology.

with respect to the CCD camera. Therefore, the double-sided monolithic flexures constraining the optic must have two degrees of freedom (pitch and yaw) for the in-situ alignment of the optic with the reference surface. This is accomplished by the use of the flexure tilt stage, a precision, vertical tilt stage that captures the three double-sided flexures, as shown in Figure 4-29.

To allow for pitch and yaw adjustments, three fine-pitch screws (1/4-80) are attached to the stage, pushing against the stationary assembly behind the tilt stage. Next to each screw, a clearance hole is provided for another bolt to go through the stage and thread into the assembly. A spring is compressed between this bolt and the

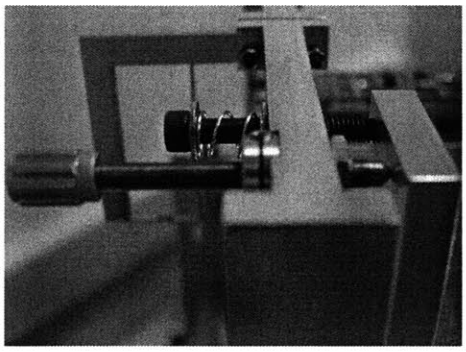

Figure 4-30: One of the three 1/4-80 screws with another bolt that threads into the structure behind the flexure tilt stage. A spring is compressed between this bolt and the stage. To restrict the lateral and vertical translation of the entire stage, two grooves are machined at the contact between the ball at the tip of the adjustment screw and the lower base (not shown) to form a ball and socket joint.

stage; therefore, the stage can not move toward the stationary structure because the fine-pitch screws constrain that motion, and it can not move away from the structure because of the preload force from the compressed spring that is pushing the stage toward the assembly. This preload force is controlled by how much the bolt going through the spring is threaded into the structure. Figure 4-30 shows a fine-pitch screw next to a bolt preloading a spring. To restrict the lateral and vertical translation of the entire stage, the ball tip of the fine-threaded screws mates with spherical grooves machined onto the structure to form spherical bearings, each allowing for rotation but not translation.

An autocollimator with a pitch and yaw resolution of 0.1 μm is used to take a primary reading of the reference block surface. A thick, 1/4 wave plate is placed into the device, and the flexure tilt stage precision screws are used to change the angular position of the optic until its front surface is parallel to the surface of the reference block. Upon removing and replacing the optic into the device, pitch and yaw repeatability are 1.2 and 11 μrad, which correspond to 0.25 and 2.3 arcsec, respectively. These values are much smaller than the required 70 arcsec angular (pitch) repeatability of the system.

4.2.3 Comparison Between Air Bearings and Flexures for Constraining Thin Optics

Throughout the course of this project, several strategies have been developed to minimize the effects of external forces that cause deformation of thin optics during metrology. The ideal case of using air bearings to support the optic is rigorously analyzed. An air bearing test stage is built to prove the concept.

Air bearings eliminate deformations caused by friction and thermal expansion mismatch due to lack of contact with the optic; however, the complexity of the appropriate design of a system utilizing these air bearings is a major drawback. Machining extremely smooth and flat bearing surfaces and critical assembly with tight tolerances immensely increases the cost of the device, with a high risk of bearing failure during metrology associated with pressure variation, which may lead to optic tilt angle change or imbalance. Additional air filters may be needed to avoid the clogging of the thin holes at the center of the bearing surfaces. The lateral stability of the load carrying vacuum (or magnetically) preloaded thrust bearings floating against a flat, horizontal surface is another issue that needs to be further addressed. The presence of the numerous pressure and vacuum lines restrains the mobility of the device and adds to the intricacy of the assembly.

The second concept using flexures is also fully analyzed and developed. Flexures can not completely eliminate friction and thermal expansion associated deformation due to their finite stiffness; however, appropriate design parameters are chosen to provide a desired performance. Flexure design, machining, and assembly are feasible and cost effective. The axial stiffness of the flexures is much larger than that of air bearings. Once constrained by the flexures, the possibility of optic vibration during metrology is basically eliminated, unlike the case of air bearings. Contact at the edges of the optic is unavoidable when constrained by flexures. The associated Hertz stresses may pose a problem when the entire surface of the optic is covered by nanofabricated sensitive structures that might be damaged by the ruby balls, a problem not found in the case of air bearings.

The assembly utilizes monolithic flexures to reduce thermal stresses and tube flexures to minimize friction effects. Two tilt stages are used to place the optic in the vertical plane with the aid of an inclinometer. This device has demonstrated a 55 nm peak-to-valley dynamic repeatability.

Bibliography

[1] M. Cable and J. M. Parker. *High-Performance Glasses.* Chapman and Hall, 1992.

[2] P. De Bisschop et al. Initial assessment of the impact of a hard pellicle on imaging using a 193-nm step-and-scan system. *Society of Photo-Optical Instrumentation Engineers*, 3:239–262, 2004.

[3] Harvard-Smithsonian Center for Astrophysics. Chandra xray observatory. Available at: http://chandra.harvard.edu.

[4] Prazisions Glas and Optik GmbH. Selected white float glass. Available at: http://www.pgo-online.com/intlframes/catalogindexset.html.

[5] Abrisa. Chemically strengthened glass-mechanical properties. Available at: http://www.abrisa.com/Guide/GlassStrengthening/chem-strengthened-mechanical.asp.

[6] Mario Jimenez-Garate. *The Development of Hard X-ray Telescope Optics and a Theoretical Model of X-ray Emission from Accretion Disks.* PhD thesis, Columbia University, Graduate School of Arts and Sciences, 2001.

[7] George W. Morey. *Properties of Glass.* Reinhold Publishing Corporation, 1954.

[8] Craig R. Forest et al. Metrology of thin transparent optics using Shack-Hartmann wavefront sensing. *Optical Engineering*, 43:742–753, 2003.

[9] Olivier Mongrard. High-accuracy foil optics for x-ray astronomy. Masters thesis, Massachusetts Institute of Technology, Department of Aeronautics and Astronautics, 2001.

[10] Drew Devitt. "Air" on the side of smoothness. *Machine Design*, 2003.

[11] Alexander H. Slocum. *Precision Machine Design.* Society of Manufacturing Engineers, 1992.

[12] U. M. S. Costa et al. Inertial effects on fluid flow through disordered porous media. *Physical Review Letters*, 82:5249–5252, 1999.

[13] Y. B. P. Kwan and J. Corbett. Porous aerostatic bearings-an updated review. *Wear*, 222:69–73, 1998.

[14] Ascher H. Shapiro. *The Dynamics and Thermodynamics of Compressible Fluid Flow.* Ronald Press Co., 1954.

[15] Murilo D. M. Innocentini et al. Permeability of refractory castables at high temperatures. *Journal of the American Ceramic Society*, 84:645–647, 2001.

[16] B. C. Majumdar and J. Schmidt. Design of externally pressurized rectangular porous thrust bearings. *Wear*, 32:1–8, 1975.

[17] H. Mori, H. Yabe, and T. Shibayama. Theoretical solution as a boundary problem for externally pressurized porous gas-bearings. *Journal of Basic Engineering*, pages 622–630, 1965.

[18] Steven C. Chapra and Raymond P. Canale. *Numerical Methods for Engineers.* McGraw-Hill, 1998.

[19] M. F. Chen and Y. T. Lin. Static behavior and dynamic stability analysis of grooved rectangular aerostatic thrust bearings by modified resistance network method. *Tribology International*, 35:329–338, 2002.

[20] Wole Soboyejo. *Mechanical Properties of Engineered Materials.* Marcel Dekker, Inc., 2003.

[21] John Casstevens et al. Silicon carbide high performance optics: A cost-effective, flexible fabrication process. *Proc. of SPIE*, 4451:458–467, 2001.

[22] A.R. Boccaccinin and Z. Fan. A new approach for the young's modulus-porosity correlation of ceramic materials. *Ceramics International*, 23:239–245, 1997.

[23] Z. Fan et al. Microstructural characterisation of two phase materials. *Material Science Technology*, 9:1094–1100, 1993.

[24] Michael F. Ashby and Harold J. Frost. *Deformation-Mechanism Maps: The Plasticity and Creep of Metals and Ceramics.* Pergamon Press, 1982.

[25] Mikell P. Groover. *Fundamentals of Modern Manufacturing: Materials, Processes, and Systems.* John Wiley and Sons, Inc., 2002.

[26] Marc Madou. *Fundamentals of Microfabrication.* CRC Press, 1997.

[27] Richter Precision Inc. Chemical vapor deposition coatings, technical data. Available at: http://www.richterprecision.com.

[28] Omley Industries. Special application brazing. Available at: http://www.omley.com.

[29] Craig R. Forest. X-ray telescope foil optics: Assembly, metrology, and constraint. Masters thesis, Massachusetts Institute of Technology, Department of Mechanical Engineering, 2003.

[30] Craig R. Forest et al. Metrology of thin transparent optics using Shack-Hartmann wavefront sensing. *Society of Photo-Optical Instrumentation Engineers*, 43:742–753, 2004.

[31] Craig R. Forest et al, Mireille Akilian, and Mark L. Schattenburg. Thin glass optic and silicon wafer deformation and kinematic constraint. *Proc. of the 18th Annual Meeting ASPE*, 30:39–42, 2003.

[32] Wayne R. Moore. *Foundations of Mechanical Accuracy.* Bridgeport, 1970.

[33] Automation Creations Inc. Material property data. Available at: http://www.matweb.com.

[34] John A. Roberson and Clayton T. Crowe. *Engineering Fluid Mechanics.* Wiley, 1997.

[35] Joseph B. Franzini and E. John Finnemore. *Fluid Mechanics with Engineering Appliations.* McGraw-Hill, 1997.

[36] Robert C. Junivall and Kurt M. Marshek. *Fundamentals of Machine Component Design.* Wiley, 1999.

[37] W. A. Gross. *Gas Film Lubrication.* Wiley, 1962.

[38] Haruo Mori. A theoretical investigation of pressure depression in externally pressurized gas-lubricated circular thrust bearings. *Journal of Basic Engineering*, 83:201–208, 1961.

[39] A. K. Stiffler. Analysis of the stiffness and damping of an inherently compensated, multiple-inlet, circular thrust bearing. *Journal of Lubrication Technology*, 96:329–336, 1974.

[40] Yunus A. Cengel. *Heat Transfer: A Practical Approach.* McGraw-Hill, 1998.

[41] Raymond J. Roark. *Roark's Formulas for Stress and Strain.* McGraw-Hill, 1989.

[42] M. Van Voorhis. Simply supported beam with twin loads, 1999. Available at: http://ourworld.compuserve.com/homepages/MJVanVoorhis/T309.htm.